ACS APPLIED ENERGY MATERIALS

www.acsaem.org Article

Double Flame-Fabricated High-Performance $AlPO_4/LiMn_2O_4$ Cathode Material for Li-Ion Batteries

Haipeng Li, Collins Erinmwingbovo, Johannes Birkenstock, Marco Schowalter, Andreas Rosenauer, Fabio La Mantia, Lutz Mädler, and Suman Pokhrel*

Cite This: *ACS Appl. Energy Mater.* 2021, 4, 4428−4443 Read Online

ACCESS | Metrics & More | Article Recommendations | Supporting Information

ABSTRACT: The spinel $LiMn_2O_4$ (LMO) is a promising cathode material for rechargeable Li-ion batteries due to its excellent properties, including cost effectiveness, eco-friendliness, high energy density, and rate capability. The commercial application of $LiMn_2O_4$ is limited by its fast capacity fading during cycling, which lowers the electrochemical performance. In the present work, phase-pure and crystalline $LiMn_2O_4$ spinel in the nanoscale were synthesized using single flame spray pyrolysis via screening 16 different precursor−solvent combinations. To overcome the drawback of capacity fading, $LiMn_2O_4$ was homogeneously mixed with different percentages of $AlPO_4$ using versatile multiple flame sprays. The mixing was realized by producing $AlPO_4$ and $LiMn_2O_4$ aerosol streams in two independent flames placed at 20° to the vertical axis. The structural and morphological analyses by X-ray diffraction indicated the formation of a pure LMO phase and/or $AlPO_4$-mixed $LiMn_2O_4$. Electrochemical analysis indicated that LMO nanoparticles of 17.8 nm (d_{BET}) had the best electrochemical performance among the pure LMOs with an initial capacity and a capacity retention of 111.4 mA h g^{-1} and 88% after 100 cycles, respectively. A further increase in the capacity retention to 93% and an outstanding initial capacity of 116.1 mA h g^{-1} were acquired for 1% $AlPO_4$.

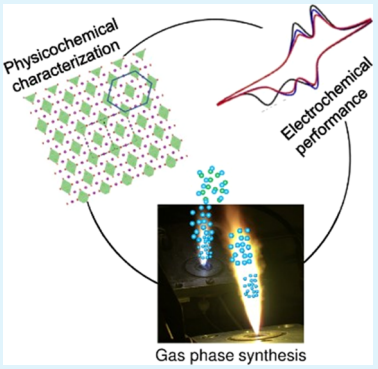

KEYWORDS: *double flame spray pyrolysis, Li-ion battery, $AlPO_4$-mixed $LiMn_2O_4$ nanoparticles, cyclic voltammetry, initial capacity, capacity retention*

INTRODUCTION

It is estimated that 10−20 million electric cars/year will enter the market by 2025 and that the use of rare transition metals including Co and Ni (main metal groups used for the battery fabrication) are in the verge of becoming scarce and very expensive (a car battery with a 100 kg cathode requires 6−12 kg of cobalt and 36−48 kg of nickel where the price of these metals has increased by ≥50% since 2015).[1] Such electric vehicles require cost-effective rechargeable batteries demonstrating high energy density and high charge/discharge rate capability.[2] To meet this demand, alternative battery materials based on more abundant transition metals are extensively researched.[1,3] Cathodic materials with inherent high operating potential, capacity, and rate capability are key to the next-generation safe and durable rechargeable lithium-ion batteries for their application in electric vehicles and devices. Among the different families of lithium-ion batteries, low-cost, high operating potential, and eco-friendly $LiMn_2O_4$ (LMO) is a promising candidate due to the presence of Mn^{3+}/Mn^{4+} redox couple in its spinel coordination.[4−6] This $LiMn_2O_4$ spinel crystallizes in a cubic system with a space group symmetry $Fd\bar{3}m$, where Li, Mn, and O occupy 8a sites with a tetrahedral coordination by oxygen, 16d sites with an octahedral coordination by oxygen, and 32e sites, respectively. The ordered Mn_2O_4 edge-shared hosts possess an open framework channel allowing three-dimensional Li diffusion.[7] The Li (de-) insertion to and/or from 8a sites occurs at 4 V maintaining the cubic spinel symmetry. It must be noted that excess Li insertion in cubic $LiMn_2O_4$ would give rise to tetragonal $Li_2Mn_2O_4$. Such a cubic−tetragonal Jahn−Teller distortion (~6.5% due to increased volume) results in the collapse of the electrode structure during charge/discharge cycling and gives rise to rapid capacity decline.[7,8] The dissolution of Mn^{2+} in the electrolyte via the disproportionation reaction ($2Mn^{3+} \rightarrow Mn^{2+} + Mn^{4+}$), formation of multiple Li−Mn−O phases, loss of material crystallinity, and microstrain growth are causes of the capacity decline of $LiMn_2O_4$ during cycling apart from Jahn−Teller distortion.[9−12]

Several approaches are known to tackle such problems, for instance, mixing or doping and/or surface coating of $LiMn_2O_4$ nanoparticles. Such approaches reduce Mn^{2+} release in the electrolyte maintaining its structure activity relationship, that is, ion and charge transport routes are undisturbed on the electrochemically active layers.[13−16] During the $Li_{1+x}Mn_{2-x}O_4$

Received: January 4, 2021
Accepted: April 6, 2021
Published: April 27, 2021

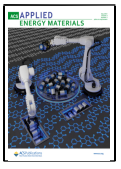

Table 1. Precursor−Solvent Combinations, Flame Parameters for the Synthesis of Pure and $AlPO_4/LiMn_2O_4$ Cathode Materials

	precursor−solvent combinations and flame parameters during particle synthesis						
	*metal concentration (L/mol)						
sample	Mn	Li	Al	liquid flow (mL/min)	dispersant O_2 flow (L/min)	premixed gas flow ($CH_4 + O_2$) L/min	abbreviation
				Single Flame			
$LiMn_2O_4$	0.274	0.137	0	3	7	1.5 + 3.2	LMO (37)
$LiMn_2O_4$	0.274	0.137	0	5	5	1.5 + 3.2	LMO (55)
$LiMn_2O_4$	0.274	0.137	0	7	3	1.5 + 3.2	LMO (73)
				Double Flame			
1% $AlPO_4$ + $LiMn_2O_4$	0.274	0.137	0.002	7	3	1.5 + 3.2	1P-LMO
2% $AlPO_4$ + $LiMn_2O_4$	0.274	0.137	0.004	7	3	1.5 + 3.2	2P-LMO
3% $AlPO_4$ + $LiMn_2O_4$	0.274	0.137	0.006	7	3	1.5 + 3.2	3P-LMO
4% $AlPO_4$ + $LiMn_2O_4$	0.274	0.137	0.008	7	3	1.5 + 3.2	4P-LMO
5% $AlPO_4$ + $LiMn_2O_4$	0.274	0.137	0.011	7	3	1.5 + 3.2	5P-LMO
5% $AlPO_4$ + $LiMn_2O_4$	0.274	0.137	0.011	3	7	1.5 + 3.2	5P-LMO (37)

	physicochemical properties of particles obtained via FSP						
	physicochemical properties of particles			Rietveld refinement of the XRD patterns			cubic cell parameters (Å)
sample	SSA (m^2g^{-1})	d_{BET} (nm)	d_{XRD} (nm)	R_p	R_{wp}	GOF	$a = b = c$ (Å)
			Single Flame				
$LiMn_2O_4$ [LMO (37)]	175.6	8.0	3.6	1.10	1.40	1.76	8.21062
$LiMn_2O_4$ [LMO (55)]	150.1	9.3	6.7	1.23	1.56	2.19	8.22103
$LiMn_2O_4$ [LMO (73)]	78.6	17.8	12.9	1.15	1.50	2.08	8.22603
$AlPO_4$	85.1	27.4					
			Double Flame				
1% $AlPO_4$ + $LiMn_2O_4$ [1P-LMO]	79.1	17.8	14.0	1.31	1.64	1.27	8.23815
2% $AlPO_4$ + $LiMn_2O_4$ [2P-LMO]	74.2	19.0	13.0	1.35	1.69	1.36	8.23923
3% $AlPO_4$ + $LiMn_2O_4$ [3P-LMO]	67.5	21.0	12.7	1.31	1.64	1.27	8.23920
4% $AlPO_4$ + $LiMn_2O_4$ [4P-LMO]	72.9	19.5	12.4	1.32	1.66	1.29	8.23911
5% $AlPO_4$ + $LiMn_2O_4$ [5P-LMO]	64.0	22.3	12.3	1.29	1.62	1.24	8.23898
5% $AlPO_4$ + $LiMn_2O_4$ [5P-LMO (37)]	195.5	7.3					

(x = 0 to 1/3) synthesis, the variable composition non-stoichiometry is possible due to the variable oxidation states of Mn^{3+} and Mn^{4+} when x = 0 and 1/3, respectively.[15] While unavoidable electrochemically inactive multiple phases occur during sintering, new synthetic techniques enabling highly crystalline and stoichiometric $LiMn_2O_4$ are required.[17] Besides hindering Mn ion dissolution, reducing the particle size of $LiMn_2O_4$ is also a promising approach to overcome such capacity decline.[12,18,19] In addition, using nanoparticles with large specific surface areas as electrodes increases the contact area with the electrolyte and enhances electronic and lithium transport via short path lengths, which gives rise to the improvement of charge/discharge rates and significant reduction of diffusion limitations, respectively.[20−23] Flame spray pyrolysis (FSP) is a single-step technique to strategically design ultra-pure energy storage materials,[22,24−27] mixed, doped or functionalized,[28−32] sensing, catalytic,[33−37] and nanomedical materials[30,38] or high-performance harvesting. In the present work, we report pure and $AlPO_4$-mixed $LiMn_2O_4$ focused on reducing inherent properties such as Mn^{2+} release in the electrolyte and the particle sizes for harvesting enhanced electrochemical performance.

EXPERIMENTAL SECTION

FSP Synthesis of Pure $LiMn_2O_4$ and $LiMn_2O_4/AlPO_4$ Nanocomposites. The cathode materials including $LiMn_2O_4$ and $LiMn_2O_4/AlPO_4$ were synthesized using single and double FSP, respectively (see Figure S1).

For the synthesis of $LiMn_2O_4$ (Li/Mn ratio of 1/2), 6 g of Mn(III)-acetylacetonate (Mn(III)AA, 99% purity, Sigma-Aldrich) was dissolved in 20 mL of toluene (99% purity, VWR) and 0.9 g of lithium acetylacetonate (LAA, 97% purity, Sigma-Aldrich) dissolved in 40 mL of 2-ethylhexanoic acid (99% purity, Sigma-Aldrich) were mixed together.[39,40] The precursor−solvent combination was fed into a two-fluid nozzle to form a spray flame [see Figure S1a−c].[41,42]

For the synthesis of $AlPO_4/LiMn_2O_4$ (5% $AlPO_4/LiMn_2O_4$ as a model example), 0.28 g of aluminum-tri-*sec*-butoxide (97% purity, Sigma-Aldrich) was dissolved in 43 g of xylene (97% purity, Alfa Aesar) followed by mixing with 0.19 g of triethyl phosphate (99.9% purity, Sigma-Aldrich) dissolved in 43 g of xylene. The Al and phosphate precursor−solvent combination was combusted in one independent flame while the Li and Mn precursor−solvent combination was combusted in the second independent flame [see Figure S1d]. The synthesis parameters, the sample abbreviation, and the physicochemical properties are tabulated in Table 1. The commercial $LiMn_2O_4$ particles (12057-17-9, MTI Corporation, Richmond, USA) with a specific surface area of 0.4−1.0 $m^2\ g^{-1}$ were used to compare with our gas phase-synthesized particles. Scanning electron microscopy (SEM) images of commercial LMO and LMO (73) samples are presented in Figure S2. During the flame synthesis of $LiMn_2O_4$, precursor flow rates, namely, 3, 5, and 7 mL/min with the respective flow of dispersant oxygen of 7, 5, and 3 L/min, were used. In the second flame of synthesizing $AlPO_4$, the precursor flow rate and dispersant oxygen rate were fixed at 5 mL/min and 5 L/min, respectively. For all the samples, the premixed gas flow rates of $CH_4 + O_2$ were kept constant at 1.5 + 3.2 L/min. The particles were obtained injecting the feed solution into the premixed gas flames (single flame in the case of pure $LiMn_2O_4$ and two independent flames in the case of nanocomposites) to form a fine spray. The pressure drop across the nozzle tip/s was kept constant at 1.5 bar during the synthesis

https://doi.org/10.1021/acsaem.1c00024
ACS Appl. Energy Mater. 2021, 4, 4428−4443

of LMO (37), LMO (55), and LMO (73), respectively (please see Table 1 for details). The particles were collected on a glass fiber filter with 257 mm diameter (Pall Laboratory A/F Glass) placed at a distance of 60 cm above the nozzle. During the double flame synthesis, the distance between the two nozzles was 17 cm, and the flame angle of each nozzle was kept at 20°.[43]

BET and TEM Measurements. The BET-surface adsorption measurements were conducted at the liquid N_2 temperature using a Quantachrome NOVA 4000e gas adsorption system for acquiring specific surface areas. The measurement cells with 70−100 mg of each powder were loaded in the degassing chamber and kept at 200 °C for 2 h. The data were collected by adsorbing/desorbing the known volume of the gas at a pressure (P/P_o) range of 0.01−0.90 and at a temperature of 77 K. Low- and high-resolution TEM (HRTEM) measurements were performed using a Titan 80-300 ST microscope (FEI) operated at 300 kV acceleration voltage. The microscope is equipped with an imaging corrector, an energy-dispersive X-ray (EDAX/EDX) detector, and a Tridiem Gatan imaging filter (GIF). The specimens were prepared dispersing the powder in ethanol followed by ultrasonication for 30 min. A drop of the resulting dispersant was placed on the carbon-coated Cu grids prior to the analysis. EDX spectra were recorded either by exposing the electron beam to nanoparticle agglomerates in TEM mode or by scanning the beam repeatedly over a selected rectangular region. Electron energy electron loss (EEL) spectra were recorded in diffraction mode from the regions that were selected using the selected area diffraction (SAD) aperture with the central beam centered into a spectrometer using a GIF charge-coupled device. EDX and EEL spectra were evaluated using the Thermo Fisher Scientific's TIA software package and home-written MATLAB-scripts.[44]

X-ray Diffraction and Rietveld Refinement. For all the samples listed in Table 1, powder X-ray diffraction (XRD) patterns were recorded on a PANalytical X'Pert MPD Pro diffractometer, equipped with a Cu-tube producing Ni-filtered $K\alpha_{1,2}$ radiation, a sample spinner taking 4 s per rotation, primary and secondary Soller slits (0.04 rad), and a position sensitive detector (X'Celerator with 127 channels and aperture of 0.01671°/channel). The samples were prepared in ∼0.2 mm deep and ∼14 mm wide blind holes on single-crystalline Si holders. Diffraction patterns were taken from 5 to 90° 2θ or 10 to 120° 2θ at steps of 0.01671° and step times of 220 or 200 s, respectively. No reflections were observed below 10°, so data below 10° were excluded in the Rietveld refinements using the BRASS2 program.[45,46] For the evaluation of crystallite sizes (d_{XRD}), the instrumental reflection widths were analyzed using standard LaB_6 data recorded in the same instrument. The reflection broadening parameters extrapolated to 0° 2θ were refined for the crystallite size to match extra reflection widths using a 1/cos θ-law followed by the well-known Scherrer equation.

Electrochemical Measurements. The cathodic slurries of $LiMn_2O_4$ and/or $LiMn_2O_4$/$AlPO_4$ nanoparticles were prepared in a ratio of 70:20:10 using the cathode active material, carbon C65 (Timcal, Bodio Switzerland, specific surface area: 62 $m^2\ g^{-1}$), and polyvinylidene fluoride in *N*-methyl-2-pyrrolidone (Solef S5130, Solvay), respectively. The slurries were mixed thoroughly using a ULTRA-TURRAX disperser (IKA) for 30 min followed by 10 min of stirring. Electrodes with a diameter of 10 mm were prepared by hand painting the $LiMn_2O_4$ or $LiMn_2O_4$/$AlPO_4$ nanoparticle slurries on a current collector (carbon cloth, Fuel Cell Earth). The painted electrodes were dried in a vacuum oven at 120 °C for 24 h. Electrochemical measurements were performed in a two-electrode coin-type cell configuration assembled in a glove box with $LiMn_2O_4$ as the working electrode and lithium metal as a counter/reference electrode [see Figure S3a,b]. The electrolyte was 1 M $LiPF_6$ (Merck kGA, Darmstadt, Germany) in ethylene carbonate and dimethyl carbonate (1:1). Electrochemical characterization was performed using cyclic voltammetry (CV) with a scan rate of 0.1 mV s^{-1} within a voltage range of 3.5−4.5 V versus Li/Li^+ and galvanostatic cycling with potential limitation (GCPL) on a Biologic VSP-300 instrument [see Figure S3c].

RESULTS AND DISCUSSION

Particle Synthesis. To design phase-pure $LiMn_2O_4$ particles, a series of Mn and Li precursor−solvent combinations were screened. While lithium precursors, namely, lithium nitrate, lithium tertiary butoxide, and LAA were used for the preparation of Li solutions,[27] manganese napthenate, manganese 2-ethylhexanoate [Mn(II)EHA], and Mn(III)AA were used as the Mn source (see Table S1). The phase analysis of the particles after the flame combustion of the 16 different precursor−solvent combinations produced undesired mixed phases consisting of major Mn_3O_4 (50−86 mass %) and minor $LiMn_2O_4$ phases (see Figures S4 and S5). When a manganese precursor with Mn^{3+} was used for combustion (see Table 1), phase-pure $LiMn_2O_4$ was obtained (see Figure S4, blue curve). While the high-temperature FSP is an extremely fast process, and in which, the metal vapor remains in the flame only for few ms,[47−49] the oxidation time of Mn^{2+} to Mn^{3+} and Mn^{4+} ($LiMn^{3+}Mn^{4+}O_4$ spinel) was insufficient. However, when the precursors with a higher oxidation number, for example, Mn^{3+}, were used, the oxidation time of Mn^{3+} leading to $LiMn^{3+}Mn^{4+}O_4$ was sufficient (Figure S6). The time scales of manganese oxidation are also limited by the competing particle nucleation process, which quenches manganese oxidation owing to the slower solid phase oxidation compared to fluid phase manganese. Therefore, two possible ways are proposed in the future work to promote the formation of pure phase $LiMn_2O_4$ from precursors with Mn^{2+}: (1) slowing down the particle nucleation process by delaying the fast quenching process and (2) increasing the high-flame temperature residence time to prolong the oxidation time.

The likelihood of the Mn_3O_4 formation on the $LiMn_2O_4$ surface during cycling is associated with $LiMn_2O_4$ electrode degradation and such a Mn^{2+} release (33% of Mn in Mn_3O_4 is divalent) is the highest at the charged state.[50,51] Such a metal ion release is critical while it jeopardizes the battery performance via unwanted chemical reactions. In the double flame spray combustion, the aerosol stream of the particles after the independent combustion of two precursor−solvents in each flame mix homogeneously. While each independent flame has a possibility of doping beyond the solubility limit (when flame intersect), multicomponent particle mixing is possible when both the independent flames are sufficiently apart. Hence, the use of multiple flames has advantages including specific design and controlled particle mixing and dispersion. Such multicomponent mixing can be tailored using nozzle distances as well as the intersection of the aerosol streams. The typical double flame in the experimental setting is shown in Figure S1d. The homogeneous particle mixing during double FSP is realized in three different flame conditions (1) when two independent flames intersect with one another (similar to single flame situation), (2) the two flames are not in contact, but the two aerosol streams meet at a certain distance above the flame, and (3) the two flames are very far apart and the aerosol streams meet with one another when the temperature in the intersecting point is much lower.[52−54] When the flames intersect at the point where the precursors are still in the gas phase, the atomic mixing or doping is an outcome. However, the two aerosol streams mixing in a nucleating zone with a sufficient temperature results in sintered polycrystalline particles. The longer the intersection distances, the more favorable situation is realized for the multicomponent oxide mixtures in the particle scale. When the temperature of the two aerosol mixing points is relatively lower,

https://doi.org/10.1021/acsaem.1c00024
ACS Appl. Energy Mater. 2021, 4, 4428−4443

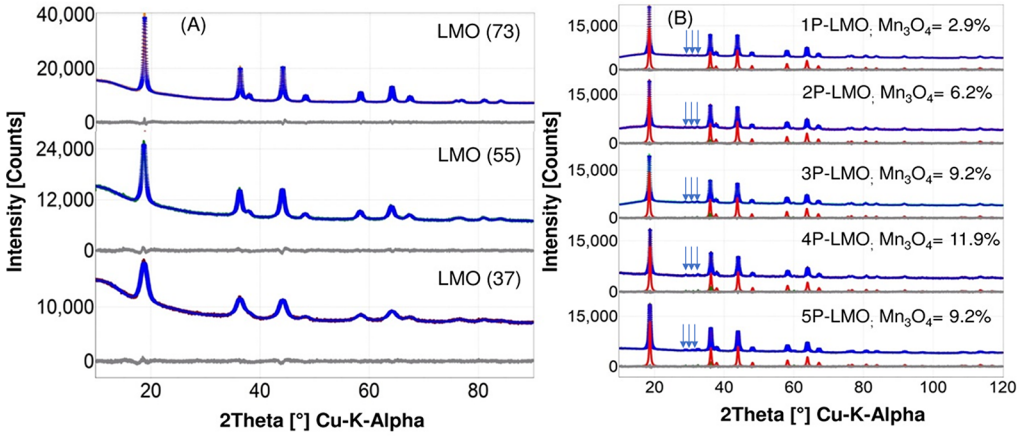

Figure 1. (A) Rietveld refinement plots of samples LMO (73), LMO (55), and LMO (37). Results show the absence of the minor Mn_3O_4 phase. (B) Rietveld refinement of samples of 1A-LMO, 2A-LMO, 3A-LMO, 4A-LMO, and 5A-LMO. Results show the presence of the minor Mn_3O_4 phase (indicative, yet not the strongest reflections (112), (020), and (013) marked by the small arrows). Although the Mn_3O_4 reflection intensities in the XRD patterns are hardly visible, the analysis resulted in significant amounts of Mn_3O_4 (2.9, 6.2, 9.2, 11.9, and 9.2 mass %) for (1, 2, 3, 4, and 5 mass %) $AlPO_4$-mixed $LiMn_2O_4$.

Table 2. Abbreviations of the Samples of Particles Used in TEM, EDX, EELS, and EFTEM Jump Ratio Map Measurements[a]

sample	liquid flow (mL/min)	dispersant O_2 flow (L/min)	abbreviation of as-prepared particles	abbreviation of particles after battery test
		Single Flame		
$LiMn_2O_4$	7	3	LMO (73)	LMO (73)_tested
		Double Flame		
1% $AlPO_4$ + $LiMn_2O_4$	7	3	1P-LMO	1P-LMO_tested
5% $AlPO_4$ + $LiMn_2O_4$	3	7	5P-LMO (37)	5P-LMO (37)_tested

[a]Herein, the precursor flow rate and the dispersant oxygen rate were used in the flame of synthesizing $LiMn_2O_4$. In the second flame of synthesizing $AlPO_4$, the precursor flow rate and the dispersant oxygen rate were fixed at 5 mL/min and 5 L/min, respectively.

the particle mixture is obtained in the agglomerate scale.[52] In this work, we exploited a second independent flame to homogeneously mix $AlPO_4$ with the $LiMn_2O_4$ aerosol stream (the distance between the two flames was kept constant at 17 cm) directly above the two flames inclined at 20° to the vertical axis, aiming at the $AlPO_4$–$LiMn_2O_4$ electrode material to outperform the state-of-the-art materials. Hence, the $AlPO_4$-mixed $LiMn_2O_4$ electrode material was designed to (1) avoid $AlPO_4$ interacting chemically with $LiMn_2O_4$, (2) stabilize the surface structure, especially to avoid any surface reconstruction or diffusion of Mn ions within the electrolyte during the charge/discharge process, and (3) exhibit thermal stability with enhanced cycle-life.[55,56]

Particle Characterization and Structural Analysis of Pure and $AlPO_4$-Mixed $LiMn_2O_4$. The specific surface areas of the pure-phase $LiMn_2O_4$ nanoparticles obtained using different dispersant O_2/feed ratios are in the range of 78.6–175.6 $m^2\ g^{-1}$ (Table 1 and Figure S7). Increasing the precursor feed rate resulted in a higher metal concentration in the spray flame and thus more nucleation seeds in the gas phase, resulting in a higher particle number density. Decreasing the dispersion oxygen rate increases the flame height (Figure S1) with a prolonged high-temperature particle residence time. With the increase in the particle number density and high-temperature residence time, the coagulation and sintering of the particle are promoted giving rise to a large particle size (low specific surface area).[6,57] The specific surface area of $AlPO_4$-mixed $LiMn_2O_4$ nanoparticles decreases only slightly with increasing the $AlPO_4$ mass fraction (Table 1 and Figure S7). The diffraction patterns of all samples (Figures 1 and S6) basically display the reflections of $LiMn_2O_4$. However, samples with $AlPO_4$ (1, 2, 3, 4, and 5 mass %) show very minor reflections at positions typical for tetragonal Mn_3O_4 (indicative, though not the strongest, reflections are marked by arrows). The starting structural models (ICSD database entries #89985 and #68174) for the Rietveld refinements were used for $LiMn_2O_4$ and Mn_3O_4, respectively.[58,59] Rietveld refinements resulted in significant amounts of Mn_3O_4 [2.9(2), 6.2(4), 9.2(4), 11.9(5), and 9.2(4) mass %] for $AlPO_4$ (1, 2, 3, 4, and 5 mass %) mixed $LiMn_2O_4$. The Mn_3O_4 fractions are seemingly quite large considering the small reflection intensities being hardly visible in the overview diffraction patterns, but the fraction of a phase is related to its reflection areas, not heights, and accordingly, the significant crystallite size-related broadening still results in large areas below those reflections explaining the significant fractions determined for Mn_3O_4. The accuracy of the calculated standard uncertainties needs to be validated. Considering a high detection limit for a phase with a strongly broadened reflection, uncertainties are expected to be largely underestimated in the usual least-squares procedure applied in Rietveld refinements. To establish the detection limit of Mn_3O_4 under these circumstances, Mn_3O_4 as a second phase (using the same crystallite size broadening parameters) was included in the refinements of the patterns with the absence of apparent Mn_3O_4 reflections. In one case [LMO (73)], the refinement yielded ~1 mass % Mn_3O_4, in the other [LMO (37)] ~1.8 mass % (Figure 1), although the reflections of Mn_3O_4 were invisible in the pattern. Hence, the calculated uncertainties of the mass fractions of Mn_3O_4 given above (0.2–0.5%) are slightly underestimated and would rather be in the reasonable range of 1 or 2%.

The significant amounts of crystalline Mn_3O_4 are present in the $AlPO_4$-mixed $LiMn_2O_4$, promoted by $AlPO_4$ (although the signals of $AlPO_4$ are absent) during the high-temperature gas-

https://doi.org/10.1021/acsaem.1c00024
ACS Appl. Energy Mater. 2021, 4, 4428–4443

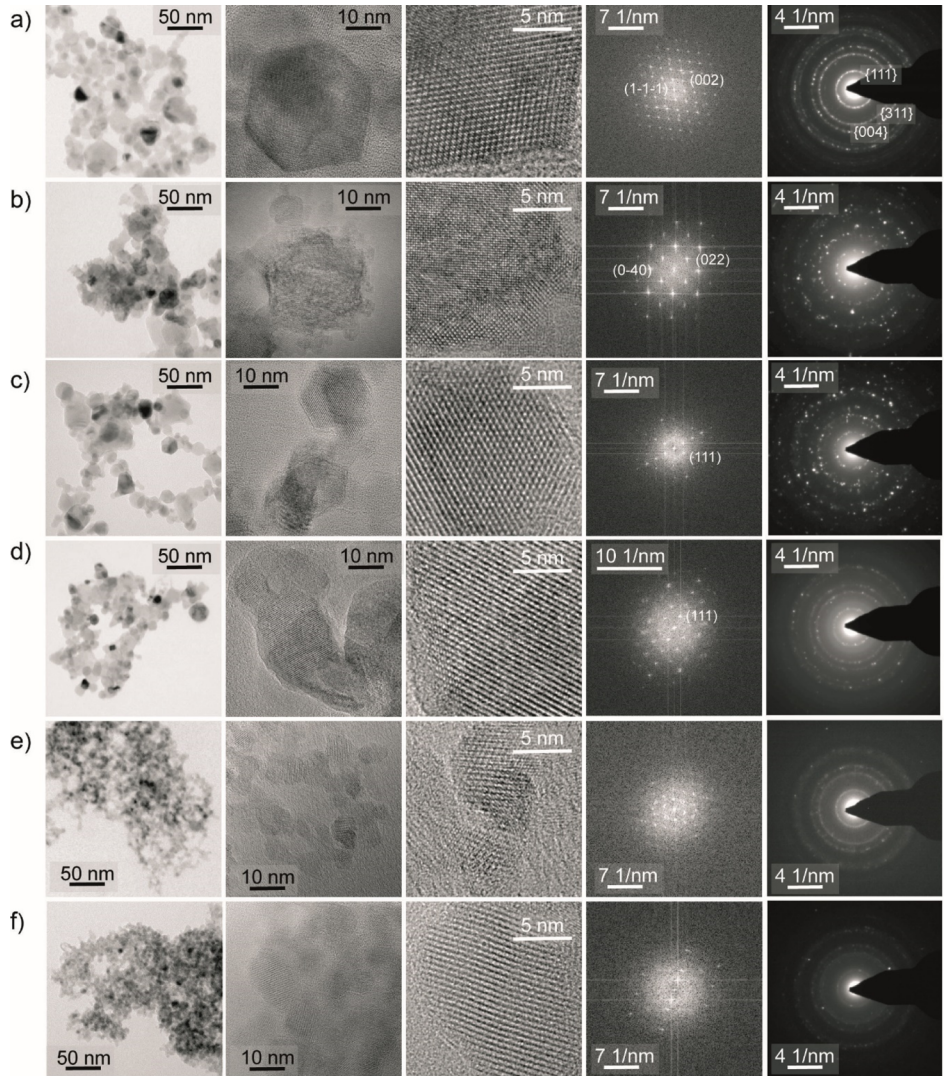

Figure 2. Comparison of TEM micrographs for the samples (a) LMO (73), (b) LMO (73)_tested, (c) 1P-LMO, (d) 1P-LMO_tested, (e) 5P-LMO (37), and (f) 5P-LMO (37)_tested. In the first two columns, overview images showing the overall morphology of the particles at medium and elevated resolution are depicted. The crystallinity of the particles can be seen in the HRTEM images in the third column. Column four displays the FFTs of approximate HRTEM images. The Debye−Scherrer diffraction patterns in column 5 were taken from agglomerates as in column 1. The analysis of the FFTs and diffraction patterns showed good agreement with the ones expected for the $LiMn_2O_4$ crystal structure.

phase synthesis (see Figure 1). The amount of $AlPO_4$ added (1−5%) during the flame synthesis is insufficient to form a "glassy hump", for example, silicate glass at low diffraction angles with a much broader extent compared to the broadened reflections of nanocrystalline phases. It must be noted that the match of the two patterns of pure and $AlPO_4$-mixed $LiMn_2O_4$ is of similar quality, for example, the difference curve in the refinements and the overall agreement indices, for example, R_p = 1.15% for the left plot and R_p = 1.14% for the right one, respectively, support the chemical composition of $LiMn_2O_4$ [Figure 1a,b].

TEM Analysis. In this subsection, TEM, EDX, EEL spectroscopy (EELS), and energy-filtered TEM (EFTEM) jump ratio map measurements were conducted on three as-prepared samples of particles and the respective samples after the battery test. Abbreviations of the investigated samples are listed in Table 2 to simplify sample names in the following text and figures.

Figure 2 shows a comparison of low-resolution images (first column) and high-resolution images (second and third column) of the samples LMO (73), LMO (73)_tested, 1P-LMO, 1P-LMO_tested, 5P-LMO (37), and 5P-LMO (37)_tested. In as-sprayed samples, small crystalline particles with facetted shapes were observed. They appear to be smaller for the "37" samples than in "73" samples. Particles in the tested samples were not only relatively small with facetted habits, but also contained portions of the material that appeared to be amorphous. The particle sizes were estimated measuring the diameter (minimum d_{min} and maximum d_{max}) for at least 100 particles in each sample (Figure S8). The particles have a diameter of roughly 19 nm with a width of the distribution of about 9 nm for LMO (73) (Figure S8). The particles obtained at a lower fuel feed rate and larger dispersant oxygen flow rate were smaller (6 nm diameter with distribution width 2 nm). The mean aspect ratio was determined to quantify the anisotropy of the particles' shape. Values of about 1.2−1.3 with a standard deviation of approximately 0.2 were found, indicating that particles are relatively isotropic in shape.

$$p_{as} = 1/N \sum_i \frac{d_{max,i}}{d_{min,i}}$$

https://doi.org/10.1021/acsaem.1c00024
ACS Appl. Energy Mater. 2021, 4, 4428−4443

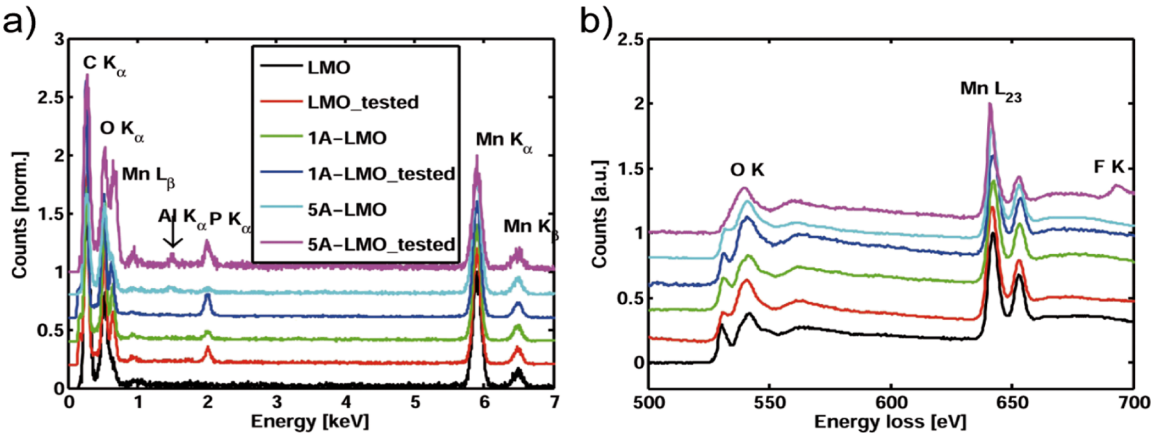

Figure 3. Comparison of (a) EDX spectra, (b) EELS O K, and Mn L_{23} spectra of particle agglomerates found in different specimens. The spectra correspond, from the bottom to top, to samples LMO (73) (black), LMO (73)_tested (red), 1P-LMO (73) (green), 1P-LMO (73)_tested (blue), 5P-LMO (37) (cyan), and 5P-LMO (37)_tested (magenta). Beside the expected Mn and O peaks, the significant additional element of F could be detected.

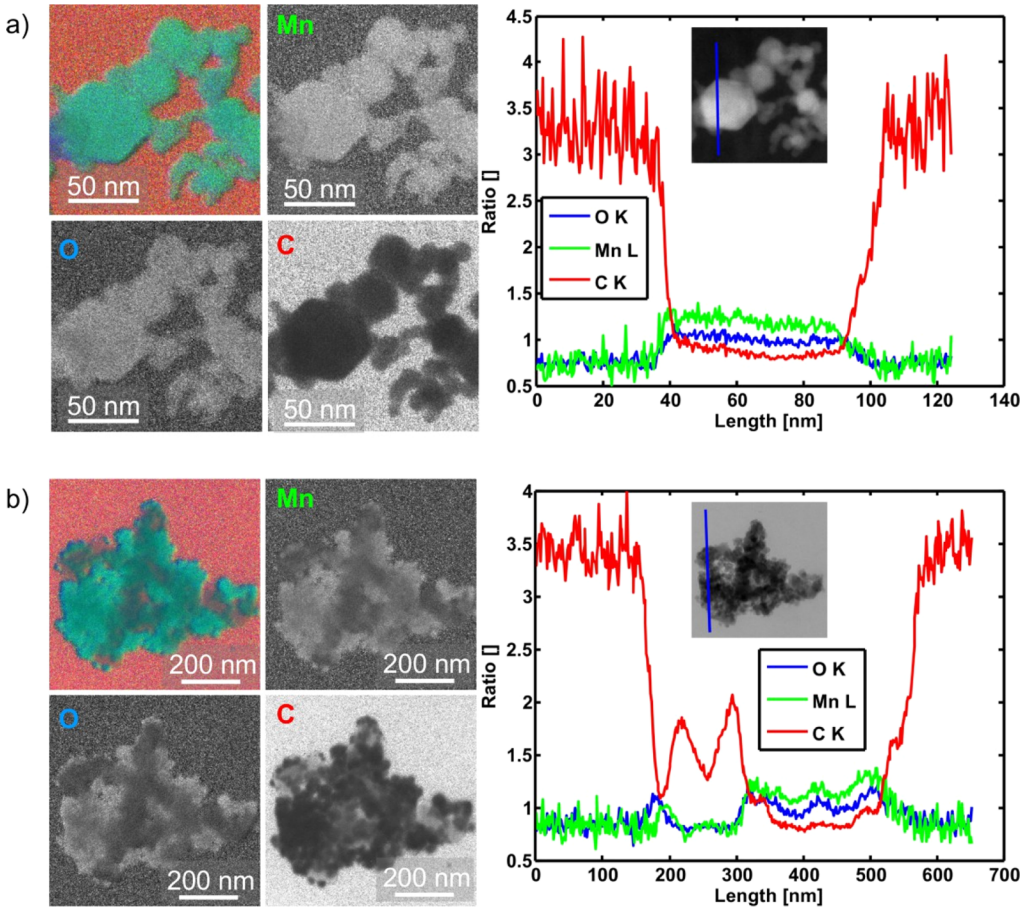

Figure 4. EFTEM jump ratio maps of the C K-, O K-, and Mn L-edge as well as a combined RGB false color map of the ratios (left column) and line scans through the agglomerates (right column) of the (a) 1P-LMO and (b) 1P-LMO_tested samples.

In order to analyze the phase of the particles, regions containing a single crystal or a part of a single crystal (similar to areas depicted in column 3 of Figure 2) were selected and fast Fourier transformed (FFTed).

The respective FFTs of the regions shown in column 3 are depicted in column 4. Distances and angles between reflections were measured for at least 6 reflections in each FFT. A series of equivalent sets of distances and angles for different zone axes were simulated based on the crystallographic information from the Rietveld refinements. The root mean square percentage deviation (RMSPD) between each simulated set and the measured data set was computed. The expected reflection positions of the set with the lowest RMSPD were superimposed on the diffractogram in order to visually check the correctness of the zone axis. Only a small rescaling of approximately 1−2% of the experimental images was needed to match diffractograms

https://doi.org/10.1021/acsaem.1c00024
ACS Appl. Energy Mater. 2021, 4, 4428−4443

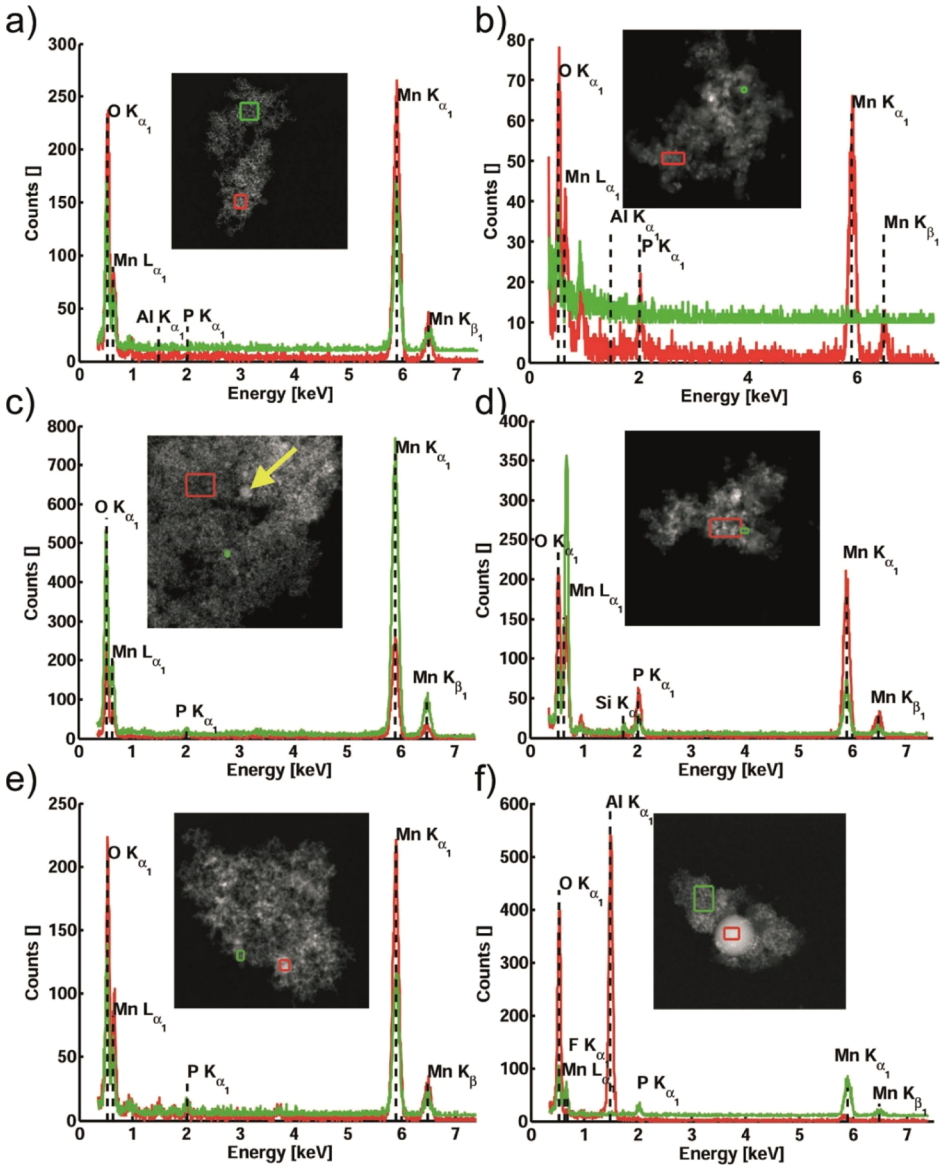

Figure 5. EDX spectra of the indicated regions for an agglomerate of (a) LMO (73), (b) LMO (73)_CV, (c) 1P-LMO (73), (d) 1P-LMO (73)_tested, (e) 5P-LMO (37), and (f) 5P-LMO (37)_tested samples. The STEM−EDX analysis showed lack of Al in most regions. In single images, large particles could be found that basically consisted of Al and O.

with the expected reflection positions. For the shown diffractograms, we found [1 1 0] and [1 0 0] zone axis orientations for the samples LMO (73) and LMO (73)_tested. In the remaining samples, particles that were not aligned in the low-indexed zone axis orientation were imaged, so the respective zone axis is missing. However, the measured reciprocal distances of the systematic rows (lattice fringes) could be matched with the distances computed from the crystallographic data of $LiMn_2O_4$. Because such an analysis is challenging to perform for hundreds of particles, SAD patterns were recorded. The resulting Debye−Scherrer diffraction patterns are displayed in the fifth column of Figure 2. Azimuthally averaged radial line scans were performed and compared to the theoretical reciprocal distances. The respective indexing of the rings is shown only for the LMO (73) sample, but is also valid for the other diffraction patterns, because the distances of the rings were nearly the same, confirming the $LiMn_2O_4$ phase.

The elemental composition and distribution were investigated with EDX spectroscopy, EELS, and EFTEM. Figure 3a compares EDX spectra taken in the different specimens condensing the electron beam to agglomerates of particles, as depicted in Figure 2, first column. As expected, Mn and O are presented in all the specimens (Li is quite light and therefore has only transition energies which are too low to be detected with the used EDX setup). Astonishingly, Al peaks were invisible in neither spectrum (besides in 5P-LMO (37)_tested). Moreover, P was detected even in spectra taken from LMO (73)_tested attributing to the P diffusion from the $LiPF_6$ electrolyte after battery tests.

The Mn Lβ peak is quite large compared to its Mn Kα peak in 5P-LMO_tested, indicating that there might be an additional element present with transition energy close to the Mn L peak.[60] This additional element could be F, whose K-line overlaps with the Mn L-line considering an energy resolution of about 135 eV of the used EDX detector, and that was confirmed by further EELS measurements. The EELS spectra were recorded in the same energy range for all the samples [Figure 3b]. The data show that the additional F K-edge identified for 5P-LMO_tested

https://doi.org/10.1021/acsaem.1c00024
ACS Appl. Energy Mater. 2021, 4, 4428−4443

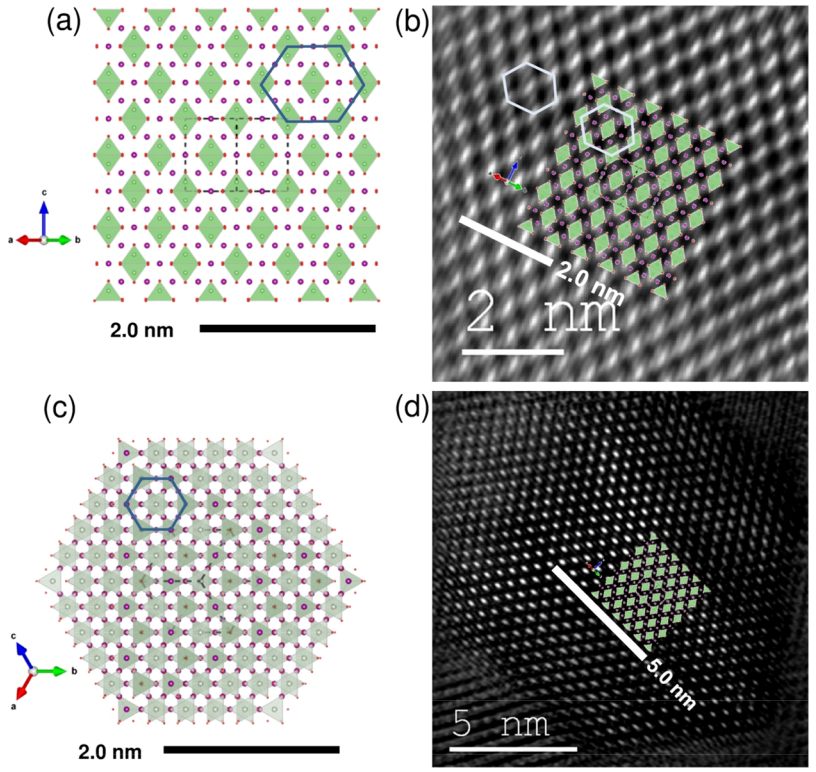

Figure 6. Crystal structure model of LMO viewed along [110] (a) and [111] (c), respectively, with respect to LMO (73) data, showing the arrangement of LiO_4 tetrahedra. Li is shown as light green atoms, LiO_4 tetrahedra in light green transparent, Mn atoms in magenta, and O atoms in red (severely reduced in size). In both projections, pseudo-hexagonal arrangements are found. However, only the one in the [110] view matches the absolute size and the distortion of the pseudo-hexagonal arrangements observed in the arrangement of light and dark contrasts in the HRTEM images of single nanocrystals of pure (b) $LiMn_2O_4$ and (d) 5P-LMO, respectively. (b) Good match is highlighted by the two distorted hexagons superimposed onto the [110] projection on the HRTEM image of pure $LiMn_2O_4$. (d) Observed regular pattern in the HRTEM image of a completely different sample 5P-LMO is again matched perfectly by the [110] projection.

was attributed to the leakage from the electrolyte ($LiPF_6$). The quantification of the Mn/O ratio from the EELS spectra (using Gatan's Digital micrograph) for the samples showed a consistent ratio of 1:2 for $LiMn_2O_4$.[15,60,61] In order to clarify such observation, EFTEM was applied (Figure 4). The data show EFTEM jump ratio maps of the C K-, O K-, and Mn L-edge as well as a RGB false colored map of agglomerates for (a) the 1P-LMO (73) and (b) the 1P-LMO_tested samples. For the 1P-LMO, the jump ratio for Mn and O is homogenously distributed in the visible particles; whereas, it is homogenously reduced for the C signal (compare also the respective line scan through the large particle). In contrast, for the 1P-LMO sample, the Mn and O signals were reduced, for example, in the middle of the agglomerate as well as in its upper left part. Exactly in these regions, the C signal increases with respect to other regions within the agglomerate. Assuming a constant thickness of the supporting C film from the TEM grid, the amorphous regions consist of a high fraction of C, which is attributed to leakages from the electrodes.

The "absence" of Al in the Al containing samples in the EDX spectra (Figure 5) was investigated switching the microscope to scanning TEM (STEM) mode. This mode has the advantage of higher sensitivity with increasing atomic number Z (the larger Z the higher the signal). However, the signal must be interpreted carefully as the intensity also depends on the thickness of the transmitted material. The regions within each of the eight agglomerates per specimen were then selected followed by moving STEM probes in the region and acquiring EDX spectra for 60 s (Figure 5). For all the agglomerates investigated in the LMO (73), the spectra looked similar with only the Mn and O signals observed [Figure 5a]. In the LMO (73)_tested sample [Figure 5b], an additional P signal was observed which originates from the electrolyte (original particles are free from P). In a region with reduced STEM intensity neither O nor Mn signals were observed, but a large C signal emerged supporting the EFTEM data (perhaps via C leakages during electrode fabrication). While 1P-LMO (as prepared and tested) showed Mn, O, and P peaks with the absence of Al signals due to only 1% $AlPO_4$ mixed in LMO, few inhomogeneously scattered spherical particles [indicated by the yellow arrow in Figure 5c], showed an Al signal (data not shown). In comparison to the 1P-LMO, a small Al signal was detected next to a P peak for 5P-LMO. The absence of Al in 1P-LMO samples outside the Al-rich particles is most likely due to the limited detection limit of the used EDX setup. In fact, EDX−SEM mapping results showed the presence of Mn, Al, and P elements in 5P-LMO (37) all over the sample (Figure S9), demonstrating the homogeneous mixing of $AlPO_4$ in $LiMn_2O_4$ particles. The quantification of the EDX spectrum yielded an atomic ratio of Al to Mn of 0.043, which is almost the same as the 0.039 in the prepared solutions during double FSP. The facts, (1) the reasonable Al/Mn atomic ratio determined for all the samples before and after the flame spray, (2) homogeneous distribution of Al in LMO particles (1−5% $AlPO_4$) observed during the EDX measurement, (3) reasonable structural match after loading $AlPO_4$ in LMO, but completely different electrochemical performance (see Electrochemical Performance section), suggest homogeneous mixing of $AlPO_4$ in $LiMn_2O_4$.

https://doi.org/10.1021/acsaem.1c00024
ACS Appl. Energy Mater. 2021, 4, 4428−4443

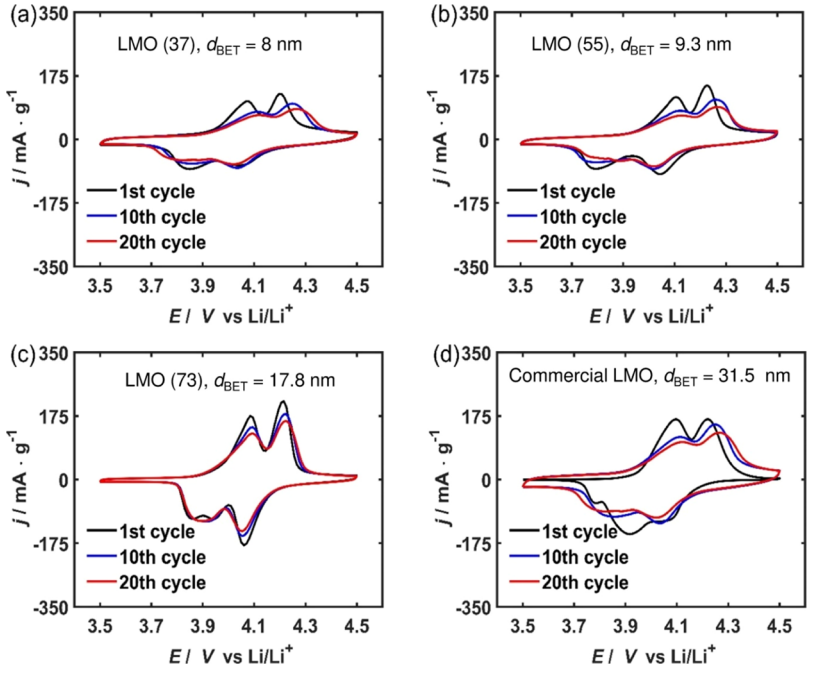

Figure 7. Cyclic voltammograms of synthesized and commercial $LiMn_2O_4$ at a scan rate of 0.1 mV s^{-1} (a) LMO (37) with a d_{BET} of 8 nm, (b) LMO (55) with a d_{BET} of 9.3 nm, (c) LMO (73) with a d_{BET} of 17.8 nm, and (d) commercial LMO with a d_{BET} of 31.5 nm. LMO (73) exhibited a well-defined peak pair compared to other LMOs and commercial LMO.

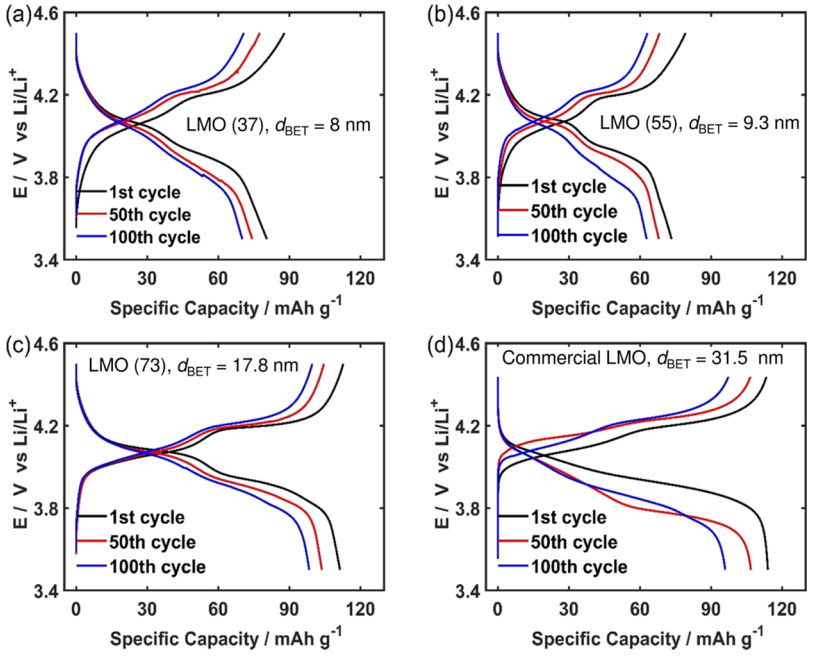

Figure 8. Charge/discharge voltage profiles of synthesized and commercial LMOs at 1 C (a) LMO (37) with a d_{BET} of 8 nm, (b) LMO (55) with a d_{BET} of 9.3 nm, (c) LMO (73) with a d_{BET} of 17.8 nm, and (d) commercial LMO with a d_{BET} of 31.5 nm. LMO (73) with d_{BET} = 17.8 nm had the highest initial capacity of the synthesized LMO with an initial capacity of 111.4 mA h g^{-1}, compared to commercial LMO (114.1 mA h g^{-1}). This reduced initial capacity of the LMO with a particle size below 17.8 nm can be attributed to the reduced fraction of vacancy sites in the bulk LMO.

Matching the Crystal Structure with 2D-Periodic Arrangements of Light and Dark Contrasts in HRTEM Images. Highly resolved TEM images of pure $LiMn_2O_4$ and $LiMn_2O_4/AlPO_4$ showed nanoparticles in the size range of 5−30 nm. The primary particles of all the samples studied were single crystals, many of them with clear lattice fringes or 2D-periodic patterns of light and dark contrasts, respectively [Figure 2]. It is most striking that the crystal projections have regular shapes with straight edges and regular angles between the edges with 2D-periodic arrangements of light and dark contrasts. The viewing is parallel to a simple crystallographic [*uvw*] direction with low *u*, *v*, and *w* indices.

In orthonormal axis systems, such as the cubic case, simple [*uvw*] directions are normal to the respective set of lattice planes [*hkl*], for example, a projection of (100) can be viewed parallel to [100]. Small angular deviations about one rotation axis

https://doi.org/10.1021/acsaem.1c00024
ACS Appl. Energy Mater. 2021, 4, 4428−4443

normal to a perfect viewing direction will lead to images with lattice fringes (alternating lines of light and dark contrast) only. A blurred image with no regular features is due to misorientation in two independent in-plane rotations (e.g., the blurred region outside of the regular crystal in Figure 6). The arrangements of light and dark contrasts in Figure 6b,d have a more or less hexagonal appearance because each bright spot is surrounded by six next-neighbor bright spots. In a cubic crystal, a perfect (yet trigonal and thus in fact "pseudo-") hexagonal arrangement would be expected for the viewing direction ⟨111⟩ looking normal to (111), as shown in Figure 6c. However, neither the absolute size of the hexagon shown here, nor its perfect regularity is observed in the arrangements of light and dark contrasts in the HRTEM images. The observed hexagons are quite distorted and larger than the ones expected for a ⟨111⟩ viewing direction. Viewing the crystal structure of LMO in other directions, the same distorted hexagon with the same absolute dimensions was observed in a direction normal to [110] (and its symmetrically equivalent *hkl* planes) when highlighting the arrangement of the LiO_4 tetrahedra (suppressing display of the oxygen polyhedra for Mn atoms). This crystal structure view, as shown in Figure 6a, matches perfectly with the observed contrast in Figure 6b,d. Note that the structures and the HRTEM images were first set on the same scale matching the 2 and 5 nm bars in the structure plot and in the HRTEM images, respectively. Then, the structure viewed in the [110] direction matches the observed contrast patterns without any further scaling. Accordingly, the much smaller, nondistorted hexagons viewed in the [111] direction is at mismatch to the observed patterns and accordingly [111] is a not the viewing direction in Figure 6b,d. The absence of structural mismatch, high and stable electrochemical performance of LMO based materials suggest efficient mixing of $AlPO_4$ in LMO.

Electrochemical Performance. The electrochemical performance of the synthesized LMO nanoparticles were investigated using CV and GCPL. Figure 7 compares the voltammograms of the synthesized $LiMn_2O_4$ with different particle sizes and commercial $LiMn_2O_4$. In all cases, it is possible to observe the typical pairs associated with the reversible (de-)insertion of lithium ions in LMO at ca. 4.2 and 3.8 V versus Li/Li^+.[62,63] The peak pair in LMO (73) was observed to be better defined, with peak separations (ΔE_p) of 150 and 180 mV, compared to the other samples [LMO (37), LMO (55), and commercial LMO]. The peak current was observed to decrease upon cycling in all LMO, which is attributed to cycle aging of the LMO. The stability of the LMO was further investigated using GCPL.

Figure 8 shows the voltage profiles of the synthesized and commercial LMO obtained at 1 C in the potential range of 3.5–4.5 V. It comprises two voltage plateaus, corresponding to the two peak pairs presenting in the cyclic voltammogram. The initial discharge capacities of LMO (37) and LMO (55) were 87.7 and 73.7 mA h g^{-1}, respectively, while LMO (73) had an initial discharge capacity of 111.4 mA h g^{-1}, which is comparable to the initial discharge capacity of commercial LMO (114.1 mA h g^{-1}). The reduced capacity observed in LMO (55) and LMO (37) is consistent with the reports in the literature, where $LiMn_2O_4$ exhibits a decrease in the discharge from 106.3 to 84.9 mA h g^{-1} as particle sizes decrease from 15.0 nm (optimal value in that case) to 6.8 nm.[39] This has been attributed to the reduced fraction of vacancy sites in the bulk of the cathode materials.[39,64] The result indicates that despite the benefits of the smaller particle size in cathode materials (enhanced charge transfer and mass transport in the solid), the reduction of the particle size of LMO below 17.8 nm tends to limit its practical usage due to the reduced capacity value. Figure 9 shows the capacity versus cycle number of the synthesized and commercial LMO. LMO (37) retained 80% of its initial discharge capacity (87.7 mA h g^{-1}) after 100 cycles while LMO (55) had a capacity retention of 86% after 100 cycles. In the case of LMO (73), its initial discharge capacities decreased from 111.4 to 98.4 mA h g^{-1}, representing a capacity retention of 88% while the initial capacity of commercial LMO decreased from 114.1 to 96.0 mA h g^{-1} representing a capacity retention of 84% after 100 cycles.

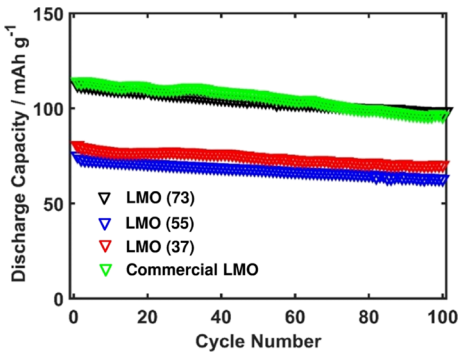

Figure 9. Cycling performance of synthesized and commercial LMO at 1 C. LMO (73) showed the superior electrochemical performance compared to the other synthesized LMO, retaining 88% of its initial discharge capacity (111.4 mA h g^{-1}) after 100 cycles.

Thus, LMO (73) had the best electrochemical performance of the synthesized LMO nanoparticles and has better cycling stability than commercial LMO. The capacity fading observed in LMO is attributed to manganese dissolution at the LMO/electrolyte interface due to the disproportionation reaction of Mn^{3+} ($2Mn^{3+} \rightarrow Mn^{4+} + Mn^{2+}$). The Mn^{2+} released from this disproportionation has been reported to deposit on the anode, thereby increasing the impedance of the cell and reducing its electrochemical performances. To circumvent this problem, the mixing of LMO (73) with different amounts of $AlPO_4$ using double FSP was explored.

Figure 10 shows the cyclic voltammogram of the $AlPO_4$-mixed LMO. The two peak pairs attributed to the reversible insertion of LMO were observed in all cases, indicating the absence of abrupt changes in the electrochemical insertion of Li^+ ions in the mixed material.

In Figure 11, the charge/discharge profile and the capacity versus cycle number for the coated LMO at different percentages of $AlPO_4$ is presented. An additional plateau at ca. 3.7 V versus Li/Li^+ was observed in the first cycle of the discharge curve in addition to the two plateaus associated with the reversible insertion of lithium in $LiMn_2O_4$. This can be attributed to the thermodynamically unstable surface of the coated LMO.[39] As the cycling continues, the surface attains thermodynamic stability, and the additional plateau becomes invisible. This phenomenon was also evident in the voltammogram, where a peak occurs at ca. 3.9 V in the first cycle and later shifts to ca. 3.7 V upon cycling. This phenomenon was already observed by Novák et al., who investigated the effect of specific combustion enthalpy on the electrochemical performance of LMO made by FSP and attributed the formation of less crystalline or defective surface due to the cooling of the particles.[39]

https://doi.org/10.1021/acsaem.1c00024
ACS Appl. Energy Mater. 2021, 4, 4428–4443

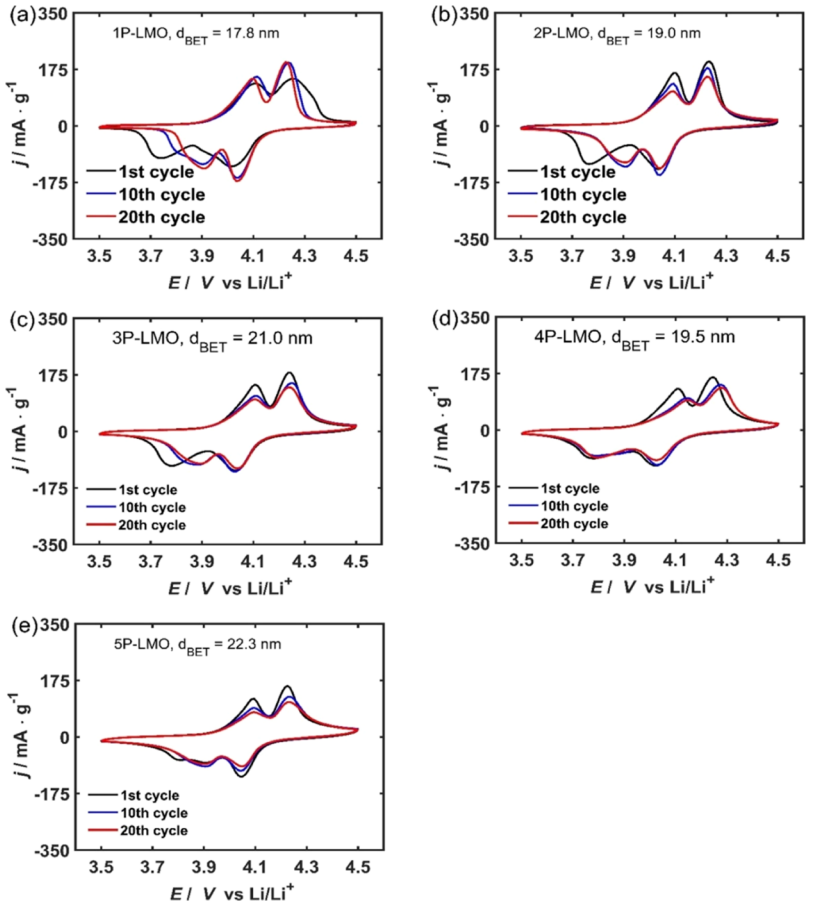

Figure 10. Cyclic voltammograms of $AlPO_4$-mixed LMO at a scan rate of 0.1 mV s^{-1} (a) 1P-LMO with a d_{BET} of 17.8 nm, (b) 2P-LMO with a d_{BET} of 19.0 nm, (c) 3P-LMO with a d_{BET} of 21.0 nm, (d) 4P-LMO with a d_{BET} of 19.5 nm, and (e) 5P-LMO with a d_{BET} of 22.3 nm. In all, the peak pairs associated with the reversible insertion of Li^+ in LMO were observed in the voltammogram, indicating no abrupt changes in the electrochemical insertion of Li^+ ions in the coated material.

The initial capacity of the mixed LMO decreases with increasing $AlPO_4$, that is, 1P-LMO, 2P-LMO, and 5P-LMO having initial discharge capacities of 116.1, 106.4, and 76.31 mA h g^{-1}, respectively (see Figure 11). This reduced capacity with increasing $AlPO_4$ content can be attributed to a decrease in Mn^{3+} with increasing $AlPO_4$ mixing.[65,66] The cycling stability of $AlPO_4$-mixed LMO is also investigated in this work, and the results obtained are shown in Figure 11f. The capacity retention of 1P-LMO after 100 cycles was 93%, superior to the bare LMO (7/3). Capacity retentions of 87 and 89% were observed for 2P-LMO and 5P-LMO, respectively. The results obtained indicate that 1P-LMO has an initial capacity similar to the bare LMO and commercial LMO, while the capacity retention after 100 cycles is 5% higher than the bare LMO (73). The latter could be due to the larger size of the 1P-LMO particles with respect to the ones of bare LMO. The rate capability of 1P-LMO is investigated, and the obtained results are shown in Figure 12. Discharge capacities of 107.7, 103.1, 88.4, and 35.28 mA h g^{-1} were obtained at 1, 2, 5, and 10 C, indicating that 1P-LMO can be cycled at 5 C at 82% of its full capacity (116.1 mA h g^{-1}). Hence, the roles of $AlPO_4$ in $LiMn_2O_4$ are (1) the strong P═O bond (5.64 eV bond energy) in the sample prevents an aggressive chemical attack to the active material during cycling.[55] (2) The high initial capacity, high retention, and outstanding stability of the $AlPO_4$-mixed $LiMn_2O_4$ is due to minimized contact area of the $LiMn_2O_4$/electrolyte interface suppressing the Mn dissolution (reduced degradation of the active material).[56]

In a recent report, Ni-doped $LiMn_2O_4$ [$Li_{1+x}Ni_{0.05}Mn_{1.95-x}O_4$ ($0 \leq x \leq 0.10$)] obtained via solution combustion was investigated for the electrochemical performance. The data showed (1) the facets (1 1 0), (1 0 0), and (1 1 1) allow favorable Li^+ ion diffusion pathways and reduce Mn dissolution, (2) the Ni-doped $LiMn_2O_4$ ($Li_{1.02}Ni_{0.05}Mn_{1.93}O_4$) exhibited reasonable electrochemical performance with initial discharge capacities of 119.8, 107.1, and 97.9 mA h g^{-1} for 1, 5, and 10 C, respectively, maintaining a capacity retention rate of 63.1%.[66] In another report, $LiMn_2O_4$ obtained using the solvothermal-lithiation process induced preferential facets such as (111), displaying high cycling stability and rate performance at extreme temperatures (−5 and 55 °C). The LMO-based materials demonstrated capacity retention and rate capability of 84.3% and 124.2 mA h g^{-1} at 10 C after 1000 cycles. While the material in the nanoscale enables Li^+ mobility for the enhancement of the rate performance, the porous structure buffers the crystal strain and unit cell volume change during Li^+ insertion/extraction. In addition, it was also reported that the preferential facet decreases the Mn dissolution during electrochemical reactions.[67] In another report, the $LiMn_2O_4$ cathode obtained using the chemical sol−gel process followed by sintering at different temperatures was tested for electrochemical performance. The high concentration of Mn^{4+} on the $LiMn_2O_4$ surface, that is, Mn^{4+}-rich surface (Mn^{4+}/Mn^{3+} was ∼2 compared to normal ratio of ∼1), was responsible for high performance. The discharge capacities at 2 and 10 C over 500 cycles were ∼110

https://doi.org/10.1021/acsaem.1c00024
ACS Appl. Energy Mater. 2021, 4, 4428−4443

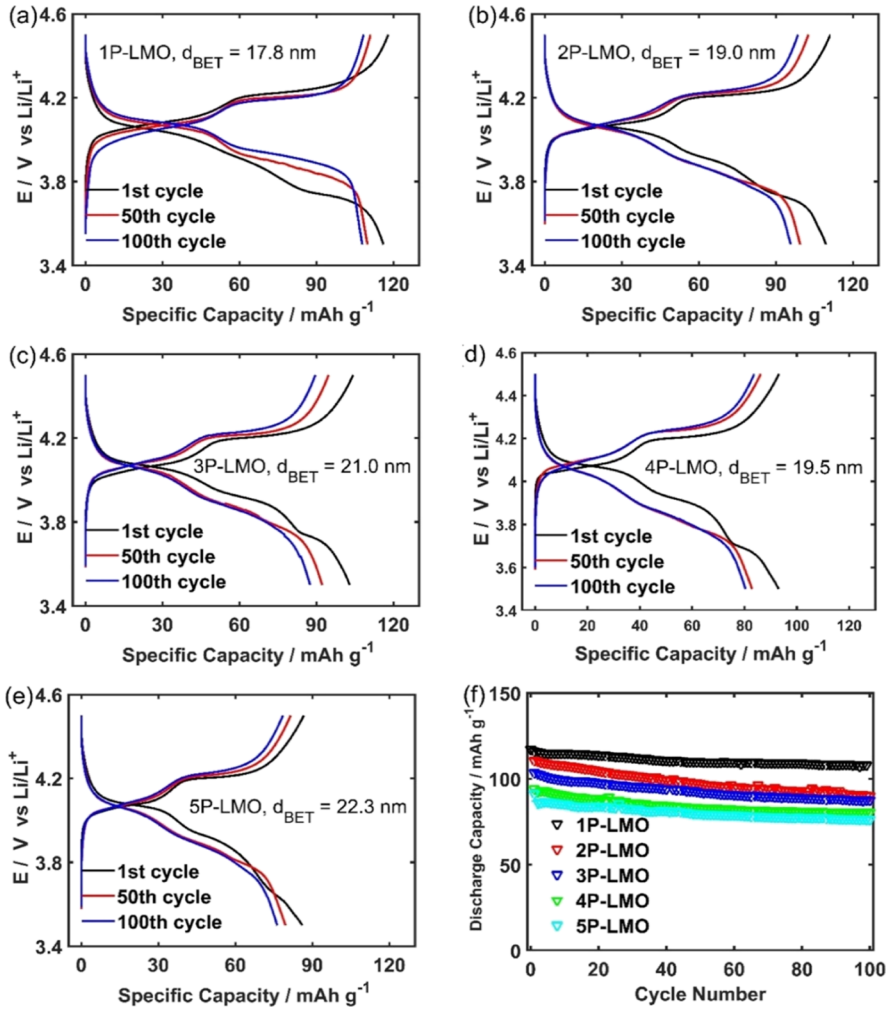

Figure 11. Charge/discharge voltage profiles of LMO mixed with different percentages of $AlPO_4$ at 1 C (a) 1P-LMO with a d_{BET} of 17.8 nm, (b) 2P-LMO with a d_{BET} of 19.0 nm, (c) 3P-LMO with a d_{BET} of 21.0 nm, (d) 4P-LMO with a d_{BET} of 19.5 nm, and (e) 5P-LMO with a d_{BET} of 22.3 nm and (f) cycling performance of LMO mixed with different percentages of $AlPO_4$ at 1 C. Increasing the percentage of $AlPO_4$ reduces the initial discharge capacities of the mixed LMO. In all, 1P-LMO showed the superior electrochemical performance in its initial capacity and a capacity retention of 93%.

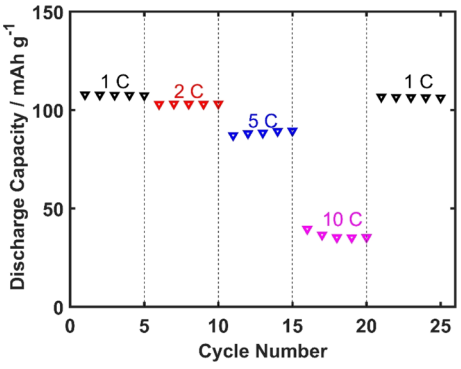

Figure 12. Rate capability of LMO mixed with 1% $AlPO_4$ at 1 C in the potential range of 3.5−4.5 V. 80% of the full capacity of 1P-LMO was obtained while cycling at 5 C.

and ∼102 mA h g^{-1}, respectively, at room temperature. Similar experiments performed at 55 °C showed 81.2 and 72% at 200 cycles for 1 and 10 C discharge rates, respectively.[68] Yang et al. synthesized the Al-rich $Li_{1.08}Al_{0.08}Mn_{1.85}Co_{0.05}O_{3.9}F_{0.1}$ (LAM-COF) cathode material using the sol−gel process followed by sintering. The Mn^{4+} concentration gradient was found to decrease from the surface to the bulk, which resulted in delivering high rate capability and good stability. The data showed 111.1 and 102.5 mA h g^{-1} and capacity retentions of 80 and 70.5% at 55 °C over 850 cycles at 1 and 5 C.[69] The aggregated and porous $LiMn_2O_4$ obtained via ball milling of the mixture of $MnCO_3$, $LiOH{\cdot}H_2O$ exhibited rate capabilities of 119, 107, and 98 mA h g^{-1} and capacity retentions of 82, 91, and 80% at 2, 10, and 20 C, respectively, for 500 cycles. Such promising results were due to the porous material, reasonable primary particle size, high crystallinity favoring rapid Li insertion/extraction kinetics, and high structural stability during the reversible electrochemical process.[70] The electrochemical performance of $LiMn_2O_4$ obtained from the FSP (reported data from FSP and present investigation) and other synthetic techniques are tabulated below and discussed (Table 3).

CONCLUSIONS

The gas-phase synthesis of spinel $LiMn_2O_4$ nanoparticles and $AlPO_4$-mixed $LiMn_2O_4$ nanoparticles was carried out using single and double FSP, respectively. To synthesize phase pure and crystalline $LiMn_2O_4$ nanoparticles, 16 various precursor−solvent combinations were tested consisting of three lithium precursors, three manganese precursors, and four solvents, and

https://doi.org/10.1021/acsaem.1c00024
ACS Appl. Energy Mater. 2021, 4, 4428−4443

Table 3. State-Of-The-Art Electrochemical Performance of $LiMn_2O_4$-Based Energy Material

material	production technique	electrochemical performance (discharge)		ref
		initial capacity	capacity retention	
$LiMn_2O_4$	FSP[a]	111.4 mA h g^{-1}, 1 C	88% (100 cycles, 1 C)	this work
$AlPO_4$-mixed $LiMn_2O_4$	FSP[a]	116.1 mA h g^{-1}, 1 C	93% (100 cycles, 1 C)	this work
		103.1 mA h g^{-1}, 2 C	82% (100 cycles, 5 C)	
		88.4 mA h g^{-1}, 5 C		
		35.28 mA h g^{-1}, 10 C		
$LiMn_2O_4$	solvothermal lithiation	137.4 mA h g^{-1}, C/2	96.4% (100 cycles, C/2)	67
$LiMn_2O_4$	solid-state reaction	112 mA h g^{-1}, C/5	85% (100 cycles, C/5)	11
$LiMn_2O_4$	one-pot resorcinol formaldehyde route	131 mA h g^{-1}, C/2	90% (100 cycles, C/2)	71
$LiMn_2O_4$	resorcinol formaldehyde route	136 mA h g^{-1}, C/5	79% at 60 C	21
$LiMn_2O_4$	FSP	102.4 mA h g^{-1}, C/5	78% (60 cycles, 50 C)	39
		108 mA h g^{-1}, 1 C		
$LiMn_2O_4$	solid-state reaction	111.9 mA h g^{-1}, C/5	89.8% (100 cycles, C/5)	51
lithium-rich $Li_{1.09}Mn_{1.91}O_4$	solid-state reaction	116 mA h g^{-1}, C/5	93% (100 cycles, C/5)	11
$LiMn_2O_4$/graphite	gel polymer electrolyte	105 mA h g^{-1}, C/5	90% (100 cycles, C/5)	4
$LiMn_2O_4$/multi-walled carbon nanotubes	low-temperature, one-pot synthesis	120 mA h g^{-1}, C/10	96% at 10 C	16
$LiMn_2O_4$/reduced graphene oxide hybrid	microwave-assisted hydrothermal method	137 mA h g^{-1}, 1 C	90% (100 cycles, 1 C)	9
$LiMn_2O_4$/carbon nanocomposites	FSP	113 mA h g^{-1}, C/2	80% at 5 C	40
		105 mA h g^{-1}, 1 C		
carbon-coated $LiMn_2O_4$	solid-state reaction	118 mA h g^{-1}, 1 C	90% (100 cycles, 1 C)	13
$AlPO_4$-coated $LiMn_2O_4$	solid-state reaction, chemical deposition method	113.2 mA h g^{-1}, C/2, 30 °C	97.4% (100 cycles, C/2)	56
P-doped $LiMn_2O_4$	wet method	78.5 mA·g^{-1}, 10 C, 55 °C	92.3% (500 cycles, 10 C, 55 °C)	65
$Li_{1.02}Ni_{0.05}Mn_{1.93}O_4$	solution combustion	119.8, 107.1, and 97.9 mA·g^{-1} at 1, 5, 10 C	91.7% (1000 cycles, 5 C)	66
microspheres and tubular $LiMn_2O_4$	solvothermal process	124.2 mA·g^{-1} at 10 C measured at −5 and 55 °C	84.3% (1000 cycles, 10 C)	67
$LiMn_2O_4$	sol−gel method	110 and 102 mA·g^{-1} at 2 and 10 C, 500 cycles, 55 °C	81.2 and 72% after 200 cycles measured at 1 and 10 C	68
$Li_{1.08}Al_{0.08}Mn_{1.85}Co_{0.0}O_{3.9}F_{0.1}$	sol−gel method	111.1 and 102.5 mA·g^{-1} after 850 cycles at 1 and 5 C	70.5% after 850 cycles at 1 C	69
porous $LiMn_2O_4$	solvothermal method	119, 107, and 98 mA·g^{-1} after 500 cycles at 2, 10, and 20 C	82, 91, and 80% after 500 cycles at 2, 10, and 20 C	70

[a]The performance of our $AlPO_4$ mixed $LiMn_2O_4$ (116.1 mA h g^{-1} at 1 C) is much better compared to the performances of other FSP materials reported (108 mA h g^{-1}, at 1 C and 105 mA h g^{-1} at 1 C).[39,40] The overall initial capacity obtained in the present investigation ranges from 111.4 to 116.1 mA h g^{-1} for pure and $AlPO_4$-mixed $LiMn_2O_4$, respectively. With respect to other synthesis methods, keeping the same C-rate (1 C), the capability of $LiMn_2O_4$ is limited to typical 120 mA h g^{-1}.[72] Compared to the other reported data shown in Table 3, the performance of our material is at the same level or even better at higher C-rates. All the electrochemical measurements were performed at room temperature and the data in the literature showing better performance are due to the testing parameter and not because of the intrinsic property of the material. In principle, the $LiMn_2O_4$-based materials obtained from FSP is at the same level or even outperforms the state-of-the-art at a higher C-rate.

the available precursor−solvent combination of Mn(III)AA−toluene + LAA−EHA was found. The manganese precursor with Mn^{3+} instead of Mn^{2+} allows phase-pure $LiMn_2O_4$ in the gas phase, which is probably caused by the short oxidation time of manganese ions in the high-temperature flame. In single FSP of $LiMn_2O_4$ nanoparticles, liquid feed rate and dispersant oxygen rate were varied to change the specific surface areas of particles (BET particle sizes). The slurries containing the prepared nanoparticles were painted on a carbon cloth current collector, which acts as the cathode electrode in the battery cell. The results demonstrated that the discharge capacity of phase-pure $LiMn_2O_4$ nanoparticles increase with the increasing of the particle size from 8.0, 9.3 to 17.8 nm. Moreover, the $LiMn_2O_4$ particles with a size of 17.8 nm have an initial discharge capacity of 111.4 mA h g^{-1}, which is comparable to the commercial particles. To overcome capacity fading and improve the electrochemical property, phase-pure $LiMn_2O_4$ particles (17.8 nm in size) with the best performance were considered to be mixed at the nanoscale with $AlPO_4$ using the versatile double FSP. For $AlPO_4$-mixed $LiMn_2O_4$ nanoparticles, the discharge capacity increases with the decreasing $AlPO_4$ from 5, 4, 3, and 2 to 1%. The optimal surface mixing of 1% $AlPO_4$ with $LiMn_2O_4$ demonstrated an energy density of 116.1 mA h g^{-1} at 1 C (almost to the typical 120 mA h g^{-1}) and a high cycling stability at 5 C with 82% of its full capacity. This work suggests FSP is a promising technique to (1) screen highly combustible precursor−solvent combination for phase-pure functional and engineered nanoparticles and (2) design ideal cathode materials for the Li-ion battery with highly promoted electrochemical performances.

https://doi.org/10.1021/acsaem.1c00024
ACS Appl. Energy Mater. 2021, 4, 4428−4443

■ ASSOCIATED CONTENT

Supporting Information

The Supporting Information is available free of charge at https://pubs.acs.org/doi/10.1021/acsaem.1c00024.

Photographs of the spray flames in the FSP synthesis of nanoparticles; precursor and solvents used in this work; SEM images of commercial LMO and LMO(73) samples; specific surface area of the FSP-synthesized mixed-phase nanoparticles using 16 precursor−solvent combinations; photographs of the battery cell; XRD patterns and Rietveld refinements of the FSP-synthesized mixed-phase nanoparticles using 16 precursor−solvent combinations; powder XRD patterns of pure and $AlPO_4$-mixed $LiMn_2O_4$ nanoparticles; BET specific surface area and BET particle diameter of three pure-phase $LiMn_2O_4$ samples and four $AlPO_4$-mixed $LiMn_2O_4$ samples; histograms of particle diameters obtained from TEM; and EDX spectrum, SEM image, and its mapping for Mn, Al, P, O, C, and Si series for the 5P-LMO(37) sample (PDF)

■ AUTHOR INFORMATION

Corresponding Author

Suman Pokhrel − *Faculty of Production Engineering, University of Bremen, 28359 Bremen, Germany; Leibniz Institute for Materials Engineering IWT, 28359 Bremen, Germany; Central Laboratory for Crystallography and Applied Materials, University of Bremen, 28359 Bremen, Germany;* orcid.org/0000-0001-5712-2824; Phone: +49 421 218-51218; Email: spokhrel@iwt.uni-bremen.de

Authors

Haipeng Li − *Faculty of Production Engineering, University of Bremen, 28359 Bremen, Germany; Leibniz Institute for Materials Engineering IWT, 28359 Bremen, Germany;* orcid.org/0000-0001-9815-1306

Collins Erinmwingbovo − *Energiespeicher- und Energiewandlersysteme, Universität Bremen, 28325 Bremen, Germany*

Johannes Birkenstock − *Central Laboratory for Crystallography and Applied Materials, University of Bremen, 28359 Bremen, Germany*

Marco Schowalter − *Institute of Solid State Physics, University of Bremen, 28359 Bremen, Germany;* orcid.org/0000-0001-5391-6934

Andreas Rosenauer − *Institute of Solid State Physics, University of Bremen, 28359 Bremen, Germany*

Fabio La Mantia − *Energiespeicher- und Energiewandlersysteme, Universität Bremen, 28325 Bremen, Germany;* orcid.org/0000-0001-7743-4198

Lutz Mädler − *Faculty of Production Engineering, University of Bremen, 28359 Bremen, Germany; Leibniz Institute for Materials Engineering IWT, 28359 Bremen, Germany;* orcid.org/0000-0002-7073-0733

Complete contact information is available at: https://pubs.acs.org/10.1021/acsaem.1c00024

Author Contributions

H.L. and C.E. contributed equally to the work. The manuscript was written through contributions of all the authors. All the authors have given approval to the final version of the manuscript.

Notes

The authors declare no competing financial interest.

■ ACKNOWLEDGMENTS

H.L., S.P., and L.M. thank the German Research Foundation (DFG) for partly funding this research within the priority program SPP 1980 SPRAYSYN under grants of MA3333/14-1 and Gottfried Wilhelm Leibniz Prize (MA3333/13-1). S.P. and L.M. would also like to thank the European Research Council (ERC) for funding part of the work under grant agreement "ReSuNiCo 786487".

■ REFERENCES

(1) Turcheniuk, K.; Bondarev, D.; Singhal, V.; Yushin, G. Ten Years Left to Redesign Lithium-Ion Batteries. *Nature* **2018**, *559*, 467−470.

(2) Kang, K.; Meng, Y. S.; Bréger, J.; Grey, C. P.; Ceder, G. Electrodes with High Power and High Capacity for Rechargeable Lithium Batteries. *Science* **2006**, *311*, 977−980.

(3) Ni, S.; Liu, J.; Chao, D.; Mai, L. Vanadate-Based Materials for Li-Ion Batteries: The Search for Anodes for Practical Applications. *Adv. Energy Mater.* **2019**, *9*, 1803324.

(4) Hu, P.; Duan, Y.; Hu, D.; Qin, B.; Zhang, J.; Wang, Q.; Liu, Z.; Cui, G.; Chen, L. Rigid−Flexible Coupling High Ionic Conductivity Polymer Electrolyte for an Enhanced Performance of $LiMn_2O_4$/Graphite Battery at Elevated Temperature. *ACS Appl. Mater. Interfaces* **2015**, *7*, 4720−4727.

(5) Lee, J.; Kitchaev, D. A.; Kwon, D.-H.; Lee, C.-W.; Papp, J. K.; Liu, Y.-S.; Lun, Z.; Clément, R. J.; Shi, T.; McCloskey, B. D.; Guo, J.; Balasubramanian, M.; Ceder, G. Reversible Mn^{2+}/Mn^{4+} Double Redox in Lithium-Excess Cathode Materials. *Nature* **2018**, *556*, 185−190.

(6) Sathiya, M.; Rousse, G.; Ramesha, K.; Laisa, C. P.; Vezin, H.; Sougrati, M. T.; Doublet, M.-L.; Foix, D.; Gonbeau, D.; Walker, W.; Prakash, A. S.; Ben Hassine, M.; Dupont, L.; Tarascon, J.-M. Reversible Anionic Redox Chemistry in High-Capacity Layered-Oxide Electrodes. *Nat. Mater.* **2013**, *12*, 827−835.

(7) Erichsen, T.; Pfeiffer, B.; Roddatis, V.; Volkert, C. A. Tracking the Diffusion-Controlled Lithiation Reaction of $LiMn_2O_4$ by In Situ TEM. *ACS Appl. Energy Mater.* **2020**, *3*, 5405−5414.

(8) Thackeray, M. M. Manganese Oxides for Lithium Batteries. *Prog. Solid State Chem.* **1997**, *25*, 1−71.

(9) Bak, S.-M.; Nam, K.-W.; Lee, C.-W.; Kim, K.-H.; Jung, H.-C.; Yang, X.-Q.; Kim, K.-B. Spinel $LiMn_2O_4$/Reduced Graphene Oxide Hybrid for High Rate Lithium Ion Batteries. *J. Mater. Chem.* **2011**, *21*, 17309−17315.

(10) Goodenough, J. B.; Park, K.-S. The Li-Ion Rechargeable Battery: A Perspective. *J. Am. Chem. Soc.* **2013**, *135*, 1167−1176.

(11) Liu, T.; Dai, A.; Lu, J.; Yuan, Y.; Xiao, Y.; Yu, L.; Li, M.; Gim, J.; Ma, L.; Liu, J.; Zhan, C.; Li, L.; Zheng, J.; Ren, Y.; Wu, T.; Shahbazian-Yassar, R.; Wen, J.; Pan, F.; Amine, K. Correlation Between Manganese Dissolution and Dynamic Phase Stability in Spinel-Based Lithium-Ion Battery. *Nat. Commun.* **2019**, *10*, 4721.

(12) Xia, H.; Luo, Z.; Xie, J. Nanostructured $LiMn_2O_4$ and Their Composites as High-Performance Cathodes for Lithium-Ion Batteries. *Prog. Nat. Sci.: Mater. Int.* **2012**, *22*, 572−584.

(13) Lee, S.; Cho, Y.; Song, H.-K.; Lee, K. T.; Cho, J. Carbon-Coated Single-Crystal $LiMn_2O_4$ Nanoparticle Clusters as Cathode Material for High-Energy and High-Power Lithium-Ion Batteries. *Angew. Chem., Int. Ed.* **2012**, *51*, 8748−8752.

(14) Lu, J.; Zhan, C.; Wu, T.; Wen, J.; Lei, Y.; Kropf, A. J.; Wu, H.; Miller, D. J.; Elam, J. W.; Sun, Y.-K.; Qiu, X.; Amine, K. Effectively Suppressing Dissolution of Manganese From Spinel Lithium Manganate Via a Nanoscale Surface-Doping Approach. *Nat. Commun.* **2014**, *5*, 5693.

(15) Schmid, H. K.; Mader, W. Oxidation States of Mn and Fe in Various Compound Oxide Systems. *Micron* **2006**, *37*, 426−432.

(16) von Bülow, J. F.; Zhang, H.-L.; Morse, D. E. Hydrothermal Realization of High-Power Nanocomposite Cathodes for Lithium Ion Batteries. *Adv. Energy Mater.* **2012**, *2*, 309−315.

(17) Paulsen, J. M.; Dahn, J. R. Phase Diagram of Li−Mn−O Spinel in Air. *Chem. Mater.* **1999**, *11*, 3065−3079.
(18) Bruce, P. G.; Scrosati, B.; Tarascon, J.-M. Nanomaterials for Rechargeable Lithium Batteries. *Angew. Chem., Int. Ed.* **2008**, *47*, 2930−2946.
(19) Lu, C.-H.; Lin, S.-W. Influence of the Particle Size on the Electrochemical Properties of Lithium Manganese Oxide. *J. Power Sources* **2001**, *97*−*98*, 458−460.
(20) Aricò, A. S.; Bruce, P.; Scrosati, B.; Tarascon, J.-M.; van Schalkwijk, W. Nanostructured Materials for Advanced Energy Conversion and Storage Devices. *Nat. Mater.* **2005**, *4*, 366−377.
(21) Chen, Y.; Xie, K.; Pan, Y.; Zheng, C. Nano-Sized $LiMn_2O_4$ Spinel Cathode Materials Exhibiting High Rate Discharge Capability for Lithium-Ion Batteries. *J. Power Sources* **2011**, *196*, 6493−6497.
(22) Ernst, F. O.; Kammler, H. K.; Roessler, A.; Pratsinis, S. E.; Stark, W. J.; Ufheil, J.; Novák, P. Electrochemically Active Flame-Made Nanosized Spinels: $LiMn_2O_4$, $Li_4Ti_5O_{12}$ and $LiFe_5O_8$. *Mater. Chem. Phys.* **2007**, *101*, 372−378.
(23) Manthiram, A.; Vadivel Murugan, A.; Sarkar, A.; Muraliganth, T. Nanostructured Electrode Materials for Electrochemical Energy Storage and Conversion. *Energy Environ. Sci.* **2008**, *1*, 621−638.
(24) Gockeln, M.; Glenneberg, J.; Busse, M.; Pokhrel, S.; Mädler, L.; Kun, R. Flame Aerosol Deposited $Li_4Ti_5O_{12}$ Layers for Flexible, Thin Film All-Solid-State Li-Ion Batteries. *Nano Energy* **2018**, *49*, 564−573.
(25) Gockeln, M.; Pokhrel, S.; Meierhofer, F.; Glenneberg, J.; Schowalter, M.; Rosenauer, A.; Fritsching, U.; Busse, M.; Mädler, L.; Kun, R. Fabrication and Performance of $Li_4Ti_5O_{12}$/C Li-Ion Battery Electrodes Using Combined Double Flame Spray Pyrolysis and Pressure-Based Lamination Technique. *J. Power Sources* **2018**, *374*, 97−106.
(26) Gockeln, M.; Ruiter, T.; Palacios Saura, A.; Baric, V.; Glenneberg, J.; Busse, M.; Pokhrel, S.; Kun, R.; Mädler, L. Enhancing the Utilization of Porous $Li_4Ti_5O_{12}$ Layers for Thin-Film Lithium-Ion Batteries. *ACS Appl. Energy Mater.* **2020**, *3*, 9667−9675.
(27) Meierhofer, F.; Li, H.; Gockeln, M.; Kun, R.; Grieb, T.; Rosenauer, A.; Fritsching, U.; Kiefer, J.; Birkenstock, J.; Mädler, L.; Pokhrel, S. Screening Precursor−Solvent Combinations for $Li_4Ti_5O_{12}$ Energy Storage Material Using Flame Spray Pyrolysis. *ACS Appl. Mater. Interfaces* **2017**, *9*, 37760−37777.
(28) George, S.; Pokhrel, S.; Ji, Z.; Henderson, B. L.; Xia, T.; Li, L.; Zink, J. I.; Nel, A. E.; Mädler, L. Role of Fe Doping in Tuning the Band Gap of TiO_2 for the Photo-Oxidation-Induced Cytotoxicity Paradigm. *J. Am. Chem. Soc.* **2011**, *133*, 11270−11278.
(29) Naatz, H.; Lin, S.; Li, R.; Jiang, W.; Ji, Z.; Chang, C. H.; Köser, J.; Thöming, J.; Xia, T.; Nel, A. E.; Mädler, L.; Pokhrel, S. Safe-by-Design CuO Nanoparticles via Fe-Doping, Cu−O Bond Length Variation, and Biological Assessment in Cells and Zebrafish Embryos. *ACS Nano* **2017**, *11*, 501−515.
(30) Naatz, H.; Manshian, B. B.; Rios Luci, C.; Tsikourkitoudi, V.; Deligiannakis, Y.; Birkenstock, J.; Pokhrel, S.; Mädler, L.; Soenen, S. J. Model-Based Nanoengineered Pharmacokinetics of Iron-Doped Copper Oxide for Nanomedical Applications. *Angew. Chem., Int. Ed.* **2020**, *59*, 1828−1836.
(31) Xiao, J.; Kuc, A.; Pokhrel, S.; Mädler, L.; Pöttgen, R.; Winter, F.; Frauenheim, T.; Heine, T. Fe-Doped ZnO Nanoparticles: The Oxidation Number and Local Charge on Iron, Studied by ^{57}Fe Mößbauer Spectroscopy and DFT Calculations. *Chem.—Eur. J.* **2013**, *19*, 3287−3291.
(32) Xiao, J.; Kuc, A.; Pokhrel, S.; Schowalter, M.; Parlapalli, S.; Rosenauer, A.; Frauenheim, T.; Mädler, L.; Pettersson, L. G. M.; Heine, T. Evidence for Fe^{2+} in Wurtzite Coordination: Iron Doping Stabilizes ZnO Nanoparticles. *Small* **2011**, *7*, 2879−2886.
(33) Kemmler, J. A.; Pokhrel, S.; Birkenstock, J.; Schowalter, M.; Rosenauer, A.; Bârsan, N.; Weimar, U.; Mädler, L. Quenched, Nanocrystalline $In_4Sn_3O_{12}$ High Temperature Phase for Gas Sensing Applications. *Sens. Actuators, B* **2012**, *161*, 740−747.
(34) Kemmler, J. A.; Pokhrel, S.; Mädler, L.; Weimar, U.; Barsan, N. Flame Spray Pyrolysis for Sensing at the Nanoscale. *Nanotechnology* **2013**, *24*, 442001.
(35) Minnermann, M.; Grossmann, H. K.; Pokhrel, S.; Thiel, K.; Hagelin-Weaver, H.; Bäumer, M.; Mädler, L. Double Flame Spray Pyrolysis as a Novel Technique to Synthesize Alumina-Supported Cobalt Fischer−Tropsch Catalysts. *Catal. Today* **2013**, *214*, 90−99.
(36) Minnermann, M.; Pokhrel, S.; Thiel, K.; Henkel, R.; Birkenstock, J.; Laurus, T.; Zargham, A.; Flege, J.-I.; Zielasek, V.; Piskorska-Hommel, E.; Falta, J.; Mädler, L.; Bäumer, M. Role of Palladium in Iron Based Fischer−Tropsch Catalysts Prepared by Flame Spray Pyrolysis. *J. Phys. Chem. C* **2011**, *115*, 1302−1310.
(37) Samerjai, T.; Tamaekong, N.; Wetchakun, K.; Kruefu, V.; Liewhiran, C.; Siriwong, C.; Wisitsoraat, A.; Phanichphat, S. Flame-Spray-Made Metal-Loaded Semiconducting Metal Oxides Thick Films for Flammable gas Sensing. *Sens. Actuators, B* **2012**, *171*−*172*, 43−61.
(38) Torres-Duarte, C.; Adeleye, A. S.; Pokhrel, S.; Mädler, L.; Keller, A. A.; Cherr, G. N. Developmental Effects of Two Different Copper Oxide Nanomaterials in Sea Urchin (Lytechinus Pictus) Embryos. *Nanotoxicol* **2016**, *10*, 671−679.
(39) Patey, T. J.; Büchel, R.; Nakayama, M.; Novák, P. Electrochemistry of $LiMn_2O_4$ Nanoparticles Made by Flame Spray Pyrolysis. *Phys. Chem. Chem. Phys.* **2009**, *11*, 3756−3761.
(40) Patey, T. J.; Büchel, R.; Ng, S. H.; Krumeich, F.; Pratsinis, S. E.; Novák, P. Flame Co-Synthesis of $LiMn_2O_4$ and Carbon Nanocomposites for High Power Batteries. *J. Power Sources* **2009**, *189*, 149−154.
(41) Dreyer, J. A. H.; Pokhrel, S.; Birkenstock, J.; Hevia, M. G.; Schowalter, M.; Rosenauer, A.; Urakawa, A.; Teoh, W. Y.; Mädler, L. Decrease of the Required Dopant Concentration for δ-Bi_2O_3 Crystal Stabilization Through Thermal Quenching During Single-Step Flame Spray Pyrolysis. *CrystEngComm* **2016**, *18*, 2046−2056.
(42) Kim, K. D.; Pokhrel, S.; Wang, Z.; Ling, H.; Zhou, C.; Liu, Z.; Hunger, M.; Mädler, L.; Huang, J. Tailoring High-Performance Pd Catalysts for Chemoselective Hydrogenation Reactions via Optimizing the Parameters of the Double-Flame Spray Pyrolysis. *ACS Catal.* **2016**, *6*, 2372−2381.
(43) Wang, Z.; Pokhrel, S.; Chen, M.; Hunger, M.; Mädler, L.; Huang, J. Palladium-Doped Silica−Alumina Catalysts Obtained From Double-Flame FSP for Chemoselective Hydrogenation of the Model Aromatic Ketone Acetophenone. *J. Catal.* **2013**, *302*, 10−19.
(44) Liu, C.; Pokhrel, S.; Tessarek, C.; Li, H.; Schowalter, M.; Rosenauer, A.; Eickhoff, M.; Li, S.; Mädler, L. Rare-Earth-Doped $Y_4Al_2O_9$ Nanoparticles for Stable Light-Converting Phosphors. *ACS Appl. Nano Mater.* **2020**, *3*, 699−710.
(45) Pokhrel, S.; Birkenstock, J.; Dianat, A.; Zimmermann, J.; Schowalter, M.; Rosenauer, A.; Ciacchi, L. C.; Mädler, L. In Situ High Temperature X-ray Diffraction, Transmission Electron Microscopy and Theoretical Modeling for the Formation of WO_3 Crystallites. *CrystEngComm* **2015**, *17*, 6985−6998.
(46) Pokhrel, S.; Birkenstock, J.; Schowalter, M.; Rosenauer, A.; Mädler, L. Growth of Ultrafine Single Crystalline WO_3 Nanoparticles Using Flame Spray Pyrolysis. *Cryst. Growth Des.* **2010**, *10*, 632−639.
(47) Li, H.; Pokhrel, S.; Schowalter, M.; Rosenauer, A.; Kiefer, J.; Mädler, L. The Gas-Phase Formation of Tin Dioxide Nanoparticles in Single Droplet Combustion and Flame Spray Pyrolysis. *Combust. Flame* **2020**, *215*, 389−400.
(48) Pokhrel, S.; Mädler, L. Flame-made Particles for Sensors, Catalysis, and Energy Storage Applications. *Energy Fuels* **2020**, *34*, 13209−13224.
(49) Schulz, C.; Dreier, T.; Fikri, M.; Wiggers, H. Gas-Phase Synthesis of Functional Nanomaterials: Challenges to Kinetics, Diagnostics, and Process Development. *Proc. Combust. Inst.* **2019**, *37*, 83−108.
(50) Jang, D. H.; Shin, Y. J.; Oh, S. M. Dissolution of Spinel Oxides and Capacity Losses in 4 V $Li/Li_xMn_2O_4$ Cells. *J. Electrochem. Soc.* **1996**, *143*, 2204−2211.
(51) Tang, D.; Sun, Y.; Yang, Z.; Ben, L.; Gu, L.; Huang, X. Surface Structure Evolution of $LiMn_2O_4$ Cathode Material upon Charge/Discharge. *Chem. Mater.* **2014**, *26*, 3535−3543.
(52) Grossmann, H. K.; Grieb, T.; Meierhofer, F.; Hodapp, M. J.; Noriler, D.; Gröhn, A.; Meier, H. F.; Fritsching, U.; Wegner, K.; Mädler,

L. Nanoscale Mixing During Double-Flame Spray Synthesis of Heterostructured Nanoparticles. *J. Nanopart. Res.* **2015**, *17*, 174.
(53) Horlyck, J.; Pokhrel, S.; Lovell, E.; Bedford, N. M.; Mädler, L.; Amal, R.; Scott, J. Unifying Double Flame Spray Pyrolysis With Lanthanum Doping to Restrict Cobalt−Aluminate Formation in Co/Al_2O_3 Catalysts for the Dry Reforming of Methane. *Catal. Sci. Technol.* **2019**, *9*, 4970−4980.
(54) Schubert, M.; Pokhrel, S.; Thomé, A.; Zielasek, V.; Gesing, T. M.; Roessner, F.; Mädler, L.; Bäumer, M. Highly Active Co-Al_2O_3-Based Catalysts for CO_2 Methanation With Very Low Platinum Promotion Prepared by Double Flame Spray Pyrolysis. *Catal. Sci. Technol.* **2016**, *6*, 7449−7460.
(55) Cho, J.; Kim, Y.-W.; Kim, B.; Lee, J.-G.; Park, B. A Breakthrough in the Safety of Lithium Secondary Batteries by Coating the Cathode Material with $AlPO_4$ Nanoparticles. *Angew. Chem., Int. Ed.* **2003**, *42*, 1618−1621.
(56) Liu, D.; He, Z.; Liu, X. Increased Cycling Stability of $AlPO_4$-Coated $LiMn_2O_4$ for Lithium Ion Batteries. *Mater. Lett.* **2007**, *61*, 4703−4706.
(57) Kelesidis, G. A.; Goudeli, E.; Pratsinis, S. E. Flame Synthesis of Functional Nanostructured Materials and Devices: Surface Growth and Aggregation. *Proc. Combust. Inst.* **2017**, *36*, 29−50.
(58) Akimoto, J.; Takahashi, Y.; Gotoh, Y.; Mizuta, S. Single Crystal X-ray Diffraction Study of the Spinel-type $LiMn_2O_4$. *Chem. Mater.* **2000**, *12*, 3246−3248.
(59) Jarosch, D. Crystal Structure Refinement and Reflectance Measurements of Hausmannite, Mn_3O_4. *Mineral. Petrol.* **1987**, *37*, 15−23.
(60) Laffont, L.; Gibot, P. High Resolution Electron Energy Loss Spectroscopy of Manganese Oxides: Application to Mn_3O_4 Nanoparticles. *Mater. Charact.* **2010**, *61*, 1268−1273.
(61) van Aken, P. A.; Liebscher, B. Quantification of Ferrous/Ferric Ratios in Minerals: New Evaluation Schemes of Fe L_{23} Electron Energy-Loss Near-Edge Spectra. *Phys. Chem. Miner.* **2002**, *29*, 188−200.
(62) Liu, W.; Kowal, K.; Farrington, G. C. Mechanism of the Electrochemical Insertion of Lithium into $LiMn_2O_4$ Spinels. *J. Electrochem. Soc.* **1998**, *145*, 459−465.
(63) Zhang, S. S.; Jow, T. R. Study of Poly(Acrylonitrile-Methyl Methacrylate) as Binder for Graphite Anode and $LiMn_2O_4$ Cathode of Li-Ion Batteries. *J. Power Sources* **2002**, *109*, 422−426.
(64) Okubo, M.; Hosono, E.; Kim, J.; Enomoto, M.; Kojima, N.; Kudo, T.; Zhou, H.; Honma, I. Nanosize Effect on High-Rate Li-Ion Intercalation in $LiCoO_2$ Electrode. *J. Am. Chem. Soc.* **2007**, *129*, 7444−7452.
(65) Hou, Y.; Chang, K.; Tang, H.; Li, B.; Hou, Y.; Chang, Z. Drastic Enhancement in the Rate and Cyclic Behavior of $LiMn_2O_4$ Electrodes at Elevated Temperatures by Phosphorus Doping. *Electrochim. Acta* **2019**, *319*, 587−595.
(66) Liu, H.; Li, M.; Xiang, M.; Guo, J.; Bai, H.; Bai, W.; Liu, X. Effects of Crystal Structure and Plane Orientation on Lithium and Nickel Co-Doped Spinel Lithium Manganese Oxide for Long Cycle Life Lithium-Ion Batteries. *J. Colloid Interface Sci.* **2021**, *585*, 729−739.
(67) Xu, C.; Li, J.; Feng, X.; Zhao, J.; Tang, C.; Ji, B.; Hu, J.; Cao, C.; Zhu, Y.; Butt, F. K. The Improved Performance of Spinel $LiMn_2O_4$ Cathode with Micro-Nanostructured Sphere-Interconnected-Tube Morphology and Surface Orientation at Extreme Conditions for Lithium-Ion Batteries. *Electrochim. Acta* **2020**, *358*, 136901.
(68) Kasireddy, S. R.; Gangaja, B.; Nair, S. V.; Santhanagopalan, D. Mn^{4+} Rich Surface Enabled Elevated Temperature and Full-cell Cycling Performance of $LiMn_2O_4$ Cathode Material. *Electrochim. Acta* **2017**, *250*, 359−367.
(69) Yang, C.; Deng, Y.; Gao, M.; Yang, X.; Qin, X.; Chen, G. High-Rate and Long-Life Performance of a Truncated Spinel Cathode Material With Off-Stoichiometric Composition at Elevated Temperature. *Electrochim. Acta* **2017**, *225*, 198−206.
(70) Deng, Y.; Zhou, Y.; Shi, Z.; Zhou, X.; Quan, X.; Chen, G. Porous $LiMn_2O_4$ Microspheres as Durable High Power Cathode Materials for Lithium Ion Batteries. *J. Mater. Chem. A* **2013**, *1*, 8170−8177.
(71) Shaju, K. M.; Bruce, P. G. A Stoichiometric Nano-$LiMn_2O_4$ Spinel Electrode Exhibiting High Power and Stable Cycling. *Chem. Mater.* **2008**, *20*, 5557−5562.
(72) Hendriks, R.; Cunha, D. M.; Singh, D. P.; Huijben, M. Enhanced Lithium Transport by Control of Crystal Orientation in Spinel $LiMn_2O_4$ Thin Film Cathodes. *ACS Appl. Energy Mater.* **2018**, *1*, 7046−7051.

https://doi.org/10.1021/acsaem.1c00024
ACS Appl. Energy Mater. 2021, 4, 4428−4443